METEOROLOGICAL OFFICE

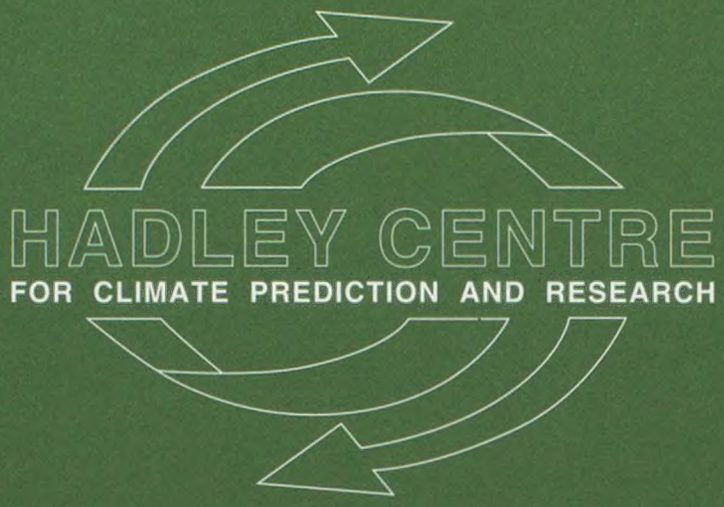

A new gravity wave drag scheme incorporating anisotropic orography and low level wave breaking : Impact upon the climate of the UK Met. Office Unified Model

by

D Gregory, G J Shutts and J R Mitchell

CRTN 75

September 1996

CLIMATE
RESEARCH
TECHNICAL
NOTE

Hadley Centre
Meteorological Office
London Road
Bracknell
Berkshire RG12 2SY

CLIMATE RESEARCH TECHNICAL NOTE NO. 75

A NEW GRAVITY WAVE DRAG SCHEME INCORPORATING ANISOTROPIC OROGRAPHY AND LOW LEVEL WAVE BREAKING: IMPACT UPON THE CLIMATE OF THE UK MET OFFICE UNIFIED MODEL

by

D Gregory, G J Shutts and J R Mitchell

Hadley Centre for Climate Prediction and Research
Meteorological Office
London Road
Bracknell
Berkshire RG12 2SY

NOTE: This paper has not been published. Permission to quote from it should be obtained from the Director of the Hadley Centre.

A new gravity wave drag scheme incorporating anisotropic orography and low level wave breaking : Impact upon the climate of the UK Met. Office Unified Model

D.Gregory[1], G.J.Shutts, J.R.Mitchell

Meteorological Office

London Road

Bracknell

Berks. RG12 2SZ

September 1996

[1]Current Affiliation : ECMWF, Shinfield Park, Reading, Berkshire, United Kingdom

Abstract

A new anisotropic gravity wave drag parametrization scheme which represents high drag states modelled on hydraulic jump, flow blocking, and internal wave reflection theory including trapped lee waves is presented. The scheme is shown to better represent the breaking of waves over mountains than previous schemes by comparison with mesoscale simulations of PYREX case studies. Extended simulations of the UK Met. Office Unified Model at climate resolution are presented, showing the impact of the new scheme and a combination of the scheme with a new orographic roughness parametrization. Results show a changed distribution of surface gravity wave surface stress mostly due to mountain anisotropy, and greater tendency for lower troposphere wave drag. Inclusion of the orographic roughness parametrization halves the gravity wave stress, the combined effect of these schemes for climate integrations being a slight improvement to the tropospheric flow.

1. Introduction

Orographically forced gravity waves play a crucial role in the momentum budget of the global circulation of the atmosphere. In the mid 1980s, inclusion of simple gravity wave drag (GWD) schemes into global circulation models, such as that described by Palmer, Shutts and Swinbank (1986), significantly reduced wind errors, particularly correcting the westerly flow bias during Northern Hemisphere winter. In Palmer et al (1986) it was assumed for convenience that most of the momentum flux was carried by long, hydrostatic plane waves and that the sub-grid scale orography is isotropic. Since then our understanding of the generation and vertical distribution of GWD has advanced, both from field studies such as PYREX (PYRenees EXperiment) and modelling. The representation of orographic roughness (OR) through the use of large effective roughness lengths (Mason, 1985; Grant and Mason, 1990) has also gained acceptance.

Although the original UK Met. Office GWD scheme of Palmer et al (1986) reduced the excessive westerly bias of both forecasts and climate models, several aspects of the scheme were clearly capable of improvement. For example the coefficient used in the estimation of gravity wave drag stress was specified at a value lower than suggested by linear gravity wave theory. It also took no account of wave trapping and assumed that the wave stress was determined by surface flow characteristics alone. The new scheme attempts to remove some deficiencies of the original scheme and improve its physical realism. New features of the revised scheme include;

(i) an assumed functional form for the orographic variance spectrum function which facilitates a crude calculation of wave drag excitation in the presence of anisotropy in the sub-grid scale orography.

(ii) a representation of high drag states (modelled on hydraulic jump response) and a treatment of the low Froude number regime (flow blocking).

(iii) internal wave reflection in the vertical together with a simple scheme for determining the occurrence of trapped lee waves which predicts their approximate wavelength and amplitude.

Recent observations of flow over the Pyrenees, together with mesoscale modelling studies are used to evaluate the performance of the new scheme. The performance of the scheme in GCM simulations is compared with the GWD scheme of Palmer et al (1986) in extended integrations (4 years in length) of the Unified Model at climate resolution. The experiments are repeated with the parametrization of orographic roughness (Smith and Jackson, 1996) included and its impact upon the activity of the gravity wave drag scheme discussed.

2. THEORETICAL OUTLINE OF REVISED GWD PARAMETRIZATION

The revised GWD scheme follows ideas presented in Shutts (1990). Details of a similar scheme that includes the effect of vertical directional wind shear may be found in Shutts (1995). The convention used here is that σ refers to standard deviation.

(i) The spectrum of orographic variances

Following the mathematical development in Bretherton (1969) and Shutts(1990,1995) we consider an isolated mountainous region within a rectangle defined by 0<x<X and 0<y<Y with h(x,y) the height of the orography equal to zero outside the rectangle. We define the double Fourier transform by:

$$\hat{h}(k,l)=\frac{1}{4\pi^2}\int_{-\infty}^{\infty}\int_{-\infty}^{\infty}h(x,y)e^{-i(kx+ly)}dxdy \qquad \hat{h}(k,l)=\hat{h}^{*}(-k,-l) \qquad)$$

where * denotes the complex conjugate. Parseval's theorem provides an expression for the mean variance since

$$\frac{1}{4\pi}\int_{-\infty}^{\infty}\int_{-\infty}^{\infty}h^2dxdy=\int_{-\infty}^{\infty}\int_{\infty}^{\infty}|\hat{h}|^2dkdl=\int_{-\infty}^{\infty}\int_{-\infty}^{\infty}A(k,l)dkdl \qquad)$$

$$where \quad A(k,l)=\frac{4\pi^2}{XY}|\hat{h}|^2$$

It would be impractical to evaluate the functional form of A(k,l) for every grid box. Instead we contrive an ensemble average estimate of the drag over a range of orographic profiles characterised by a set of orographic statistics (eg variance of height about mean). Transforming into polar co-ordinates gives,

$$\bar{A}(K)=\int_0^{2\pi} A(K,\Phi)K d\Phi \quad where\ k=K\cos\Phi\ and\ l=K\sin\Phi \qquad)$$

Bretherton (1969) suggested that this may fit a power law of the form aK^b where $-2<b<-1$. For the orography studied (in North Wales) he found $b\cong -1.5$ by computing the mean of 90 one-dimensional spectra and assuming isotropy. In mountains of West Colorado, Young and Pielke (1983) found $b\cong -1$ while in the Appalachians, Bannon and Yukas (1990) find $b\cong -1.7$. Shutts (1995) found $b=-1.5$ in the Lake District, Northern England based upon a two-dimensional spectral decomposition.

In line with these ideas, and in order to accommodate anisotropy in the representation of the orographic variance spectrum, we choose a spectrum function $A(K,\Phi) = A(K,-\Phi)$ such that,

$$K.A(K,\Phi)=\left(\frac{K_o}{K}\right)^{1.5}\left[a\cos^2\Phi+2b\sin\Phi\cos\Phi+c\sin^2\Phi\right] \qquad)$$

with $b^2 < ac$, $a>0$ and $c>0$ to ensure positivity. K_o is a constant coefficient.

If the forcing of gravity waves from sub-grid scale orography takes effect only from the part of the wave number spectrum within the annular region defined $K_L<K<K_U$, then the corresponding sub-grid scale variance σ^2 is given by:

$$\sigma^2=\int_{K_L}^{K_U}\left(\frac{K_o}{K}\right)^{1.5} dK.\int_0^{2\pi}\left[a\cos^2\Phi+2b\sin\Phi\cos\Phi+c\sin^2\Phi\right]d\Phi \qquad)$$

which simplifies to:

$$\sigma^2=2\pi K_o^{1.5}\left[K_L^{-0.5}-K_U^{-0.5}\right](a+c) \qquad (6)$$

When considering the forcing of untrapped inertia gravity waves, K_L and K_U should be limited by $K_U < N/U_\tau$ where N is the buoyancy frequency and U_τ is the generating 'surface' wind,

and $K_L > f/U_\tau$ where f is the Coriolis parameter, and provided that this wavenumber is sub-grid scale. For practical purposes we choose $2\pi/K_U \sim 10$km and $2\pi/K_L \sim 2\Delta$ where Δ is an average model grid length.

We note that

$$\frac{1}{4\pi^2}\int_0^X\int_0^Y\left(\frac{\partial h}{\partial x}\right)^2 dxdy = \int_{-\infty}^{\infty}\int_{-\infty}^{\infty} k^2|\hat{h}|^2 dkdl \qquad)$$

and define in polar form a sub-grid variance of the gradient of orography in the x-direction, σ^2_{xx}

$$\sigma^2_{xx} = \int_{K_L}^{K_U}\int_0^{2\pi} K^2\cos^2\Phi\, A(K,\Phi) K dk d\Phi \qquad)$$
$$= \frac{\pi}{6} K_o^{1.5}\left[K_U^{1.5} - K_L^{1.5}\right](3a+c)$$

Similarly,

$$\sigma^2_{yy} = \frac{\pi}{6} K_o^{1.5}\left[K_U^{1.5} - K_L^{1.5}\right](a+3c) \qquad (8b)$$

$$\sigma^2_{xy} = \frac{\pi}{3} K_o^{1.5}\left[K_U^{1.5} - K_L^{1.5}\right].b \qquad (8c)$$

(ii) Estimation of Surface Stress

Consider an airstream with constant wind speed (U_τ), buoyancy frequency N and direction (χ) flowing over irregular terrain. Following Bretherton (1969) the net momentum flux in the x-direction is given by the integral:

$$\frac{1}{XY}\int_{-\infty}^{\infty}\int_{-\infty}^{\infty} uw dxdy = -2U_o^2\int_{K_L}^{K_U}\int_{-\pi/2}^{\pi/2} K A(K,\Phi) F(K,\Phi)\cos^2(\Phi-\chi)\cos\Phi K dk d\Phi \qquad (9)$$

where the response function $F(K,\Phi)$ is given by

$$F(K,\Phi)=\frac{1}{2i|\hat{w}(K,\Phi,0)|^2}\left(\frac{\partial\hat{w}}{\partial z}\hat{w}^*-\frac{\partial\hat{w}^*}{\partial z}\hat{w}\right) \tag{10}$$

and $\hat{w}^*(K,\Phi,z)$ is the Fourier transform of the vertical velocity in polar form. In accordance with the linearized lower boundary condition,

$$\hat{w}(K,\Phi,0)=iKU_\tau\cos(\Phi-\chi)\hat{h}(K,\Phi) \tag{11}$$

Upward energy propagating solutions to the vertical structure equation for stationary gravity waves for a uniform airstream have the form

$$\hat{w}(K,\Phi,z)=c.\exp[iK(x\cos\Phi+y\sin\Phi)+il_s z] \tag{12}$$

where the hydrostatic assumption has been made and basic state density variations have been ignored so that the Scorer parameter l_s is given by,

$$l_s=\frac{N}{U_\tau\cos(\Phi-\chi)} \tag{13}$$

$F(K,\Phi)$ is easily shown to be equal to l_s. This allows the momentum flux in the x-direction to be reduced to

$$\frac{1}{XY}\int_{-\infty}^{\infty}\int_{-\infty}^{\infty}uwdxdy=-\frac{\pi U_\tau N K_o^{3/2}}{2}\left(K_U^{1/2}-K_L^{1/2}\right)(a\cos\chi+2b\sin\chi+c\cos\chi) \tag{14}$$

Use of the hydrostatic approximation will not in general be valid across the entire annular region in wavenumber space (K_L to K_U) since the vertical wave number m is given by:

$$m=(l_s^2-K^2)^{1/2}$$

and if $K > l_S$, the wave modes will be evanescent. To the level of accuracy of the parametrization scheme it will be sufficient to set K_U equal to a value for which lee waves are commonly found to be partially-trapped. Studies of lee waves over the UK have typically found such waves to have wavelengths of about 20km (e.g. Shutts (1992), Shutts and Broad (1993)). Fortuitously, the position of this cut-off in the wave number spectrum is not very

different from that of the US Navy 10' orographic data set. We suspect that the error arising from making the hydrostatic assumption will be small compared to that in other components of the parametrization scheme (e.g. the hydraulic jump regime).

Substituting with the directional variance equations (8a,b and c) gives for the x-direction,

$$\frac{1}{XY}\int_{-\infty}^{\infty}\int_{-\infty}^{\infty} uw\,dx\,dy = \frac{U_\tau N}{\hat{K}}\left(\sigma_{xx}^2\cos\chi + \sigma_{xy}^2\sin\chi\right) \qquad (15)$$

and for the y-direction,

$$\frac{1}{XY}\int_{-\infty}^{\infty}\int_{-\infty}^{\infty} vw\,dx\,dy = \frac{U_\tau N}{\hat{K}}\left(\sigma_{xy}^2\cos\chi + \sigma_{yy}^2\sin\chi\right) \qquad)$$

$$\textit{where} \quad \hat{K} = \frac{1}{3}\left[\frac{K_u^{3/2} - K_L^{3/2}}{K_u^{1/2} - K_L^{1/2}}\right] \qquad)$$

The analysis above is a generalization of the surface stress formulae used in the Palmer et al scheme but with the orographic variance replaced by combinations of σ^2_{xx},σ^2_{xy} and σ^2_{yy}.

In practical terms, high sub-grid scale orographic variances need to be artificially suppressed to account for the fact that stratified flow tends to go around rather than over steep terrain. Air may become trapped in valleys or separate near peaks thereby reducing the effective mountain height. The key non-dimensional flow parameter controlling this phenomenon is the Froude number, F_r (=U/Nh, where U is the speed of the upstream flow and h is the height of the mountain, taken to be the standard deviation of sub-grid scale orography) : flow may contain blocked layers upstream if $F_r<1$.

Another important aspect of low Froude number flow (Fr<1) over long mountain ridges is the occurrence of a hydraulic response over mountain ridges. Numerical simulations of flow over sufficiently high mountain ridges frequently exhibit strong downslope winds beneath a well mixed layer formed by wave breaking, similar to a hydraulic jump type of response (Peltier and Clark, 1979). The surface stress is considerably larger than that based on linear theory,

and the response is known as a 'high drag state'.

Smith (1995) proposed an idealised dynamical model of the high-drag flow state based on a solution of Long's equation. Although there is no intention to suggest that this model is an accurate representation of what occurs inside a model column when the Froude number is below unity, its principal features will be used to define a surface gravity wave drag formula applicable over all terrain. Perhaps the most important result used from Smith's work is that the total drag on a mountain ridge supporting the high-drag flow scales as $\varrho U^3/6N$. It is tacitly assumed that there can be only one high-drag flow state taking place within the grid-box.

Therefore based upon the requirement that for small orographic variances ($F_r >>1$) linear theory should describe the surface stress (eqns 16 and 15) and that for large variance ($F_r<1$) Smith's formula should apply, the following formulation of surface stress is used;

$$\tau_{sx}=C[\sigma_{xx}^2\cos\chi+\sigma_{xy}^2\sin\chi]$$
$$\tau_{sy}=C[\sigma_{xy}^2\cos\chi+\sigma_{yy}^2\sin\chi]$$

$$\textit{where}\quad C=\varrho K^{-1}[\frac{U_\tau^3}{N\sigma^2}].\hat{h}_1\hat{h}_2$$

$$\hat{h}_1=\begin{cases}\dfrac{N\sigma}{\alpha U_\tau} & \textit{if}<1\\ 1 & \textit{otherwise}\end{cases}$$

$$\hat{h}_2=\begin{cases}\dfrac{N\sigma}{\beta U_\tau} & \textit{if}<1\\ 1 & \textit{otherwise}\end{cases}$$

where α and β are undetermined constants, U_τ is a mean lower tropospheric wind in the direction of the surface stress and χ is the angle of wind to the westerly direction. The non-dimensional heights $\hat{h}_1$ and $\hat{h}_2$ are proportional to a notional Froude number based on the standard deviation of the sub-grid scale orography. They control the passage from the linear regime to the high drag state with respect to the Froude number and the constants α and β need to be chosen appropriately. The wind component U_τ can be determined by using eqn (18) to determine the stress vector orientation and then by resolving the wind along this direction.

Implementing eqn (18) within a large-scale model requires a 'surface' value for the wind and static stability. Wind and stability near the surface are not appropriate since the entire boundary layer may follow undulations in the terrain : the relevant values may be those just above the boundary layer top. With this uncertainty the wave 'launching height' (h_l) is defined as $(\sqrt{2})\sigma$. The surface wind and stability are then computed as averages over the height range $z=h_b$ to h_l where h_b is the height above the mean orography of a notional blocked layer. The blocked layer depth is adapted directly from the theory in Rottman and Smith (1989) i.e.

$$h_b=\sqrt{2}\sigma-(\frac{U_\tau}{N})$$

The launching height is limited to a maximum value of 1000m as with the above specification over high terrain with large sub-grid orographic varience it may reach jet stream levels.

(iii) Vertical Distribution of Stress

It is assumed for convenience, that the surface stress vector calculated from eqn (18) is due to a spectrum of hydrostatic gravity waves orientated in the direction of the surface wind. Provided the criterion for a high drag state has not been met, the surface stress equations may be used to determine the stress tolerance of any layer in the atmosphere if orographic variances are imagined to relate to the topography of an isentropic surface perturbed by a gravity wave. The saturation stress limit of the layer may be found by substituting into the

surface stress equations (eqn 18) the condition

$$\sigma = \frac{\alpha U_o}{N} \tag{19}$$

implying that $\hat{h}_1=1$ and $\hat{h}_2=\alpha/\beta$ so that C is replaced by:

$$C' = \rho K^{-1}\left[\frac{U_o^3}{N\sigma^2}\right].\frac{\alpha}{\beta} \tag{20}$$

Note that U_o is now the wind component at some height in the direction of the (surface) stress, and that χ still refers to a mean lower tropospheric wind. Hence the direction of the critical stress is that of the surface stress. If the critical stress exceeds the stress in the layer below, there is no reason for stress to be modified, and there is no drag between these layers. However when the stress carried up from below exceeds the critical stress then it is assumed the wave is unstable and partially breaks; the difference in the stresses is a drag force on the layer.

Numerical simulations and laboratory experiments have clearly shown that under certain conditions a distinctive high drag response occurs, similar to a hydraulic jump type of flow eg. Clark and Peltier (1977); Bacmeister and Pierrehumbert (1988); Rottman and Smith (1989). The hydraulic jump response describes low level wave breaking as the Froude number approaches unity from above. The value of the Froude number giving the onset of this response is $1/\alpha$, and the surface stress acquires a square dependency on U_τ. As the Froude number further reduces and falls below unity, flow blocking may accompany the hydraulic jump. This point is determined by the Froude number having a value of $1/\beta$. For flows with Froude numbers below this value the surface stress has a cubic dependency upon U_τ.

The assumption of the theory, supported by numerical simulations, is that 2/3 of the wave stress is deposited linearly with pressure from surface to a hydraulic jump height, H_o, which is taken to be 3/4 of the mean vertical wave length, following Smith (1989). If U_o/N is approximately constant with height then the jump height is defined by the condition,

$$\int_d^{H_o} \frac{N(z)}{U_o(z)} dz \geq \frac{3\pi}{2} \qquad (21)$$

At any point, if the wind has turned through $\pi/2$ from the direction of a single plane gravity wave, the wave must break entirely. It is possible that a critical layer may be found underneath the hydraulic jump height, H_o. If this is so, then *all* of the drag must be deposited below this layer, a linear reduction of stress from the 'surface' being assumed.

(iv) Partial Internal Reflection and Trapped Lee Waves

A further feature of the scheme deals with the partial internal reflection of long hydrostatic gravity waves. This is represented by a transmission coefficient, a factor by which the surface stress is reduced before its vertical attribution. Vertical variations of the Scorer parameter provide an indication of where reflection will occur. The vertical profile of this parameter is known to be very noisy even at scales much shorter than the vertical wavelength of gravity waves. This makes the nature of vertical reflection difficult to determine, and dependent on the wavelength. A variable depth two-layer model is adopted here for computational efficiency. The Scorer parameter based on model wind and temperature is calculated for each layer, the depth of the layers of equal mass being adjusted until a resonant mode is found. This model is also used to estimate the contribution to the gravity wave stress from trapped lee waves.

Referring to equations (10) and (12), trapped lee waves occur for values of K and Φ which cause $\hat{w}(K,\Phi,0)$ to tend to zero: this leads to a pronounced spike in $F(K,\Phi)$. After lengthy derivations Bretherton (1969) gives the mean vertical momentum flux at the surface due to trapped lee waves in the limit of no energy leakage out of the assumed trapped layer (Bretherton, 1969; eqn 61). In view of its fearsome nature some simplification is required. First we remove summation over all resonance branches and select only the first internal wave mode (ie. the one with no nodes). This is supported by observations, such as those of Brown (1983). The next step is to assume, in accordance with observations of lee waves, that the dominant contribution to the integral will tend to come from wave vectors of similar

orientation to the surface wind, setting $\Phi=\varkappa$. The integrand will be assumed zero outside of the range of ϕ given by $\varkappa-\Delta\Phi/2 < \Phi < \varkappa+\Delta\Phi/2$ where $\Delta\Phi$ is chosen arbitrarily and forms part of a 'tuning' constant. With these assumptions the surface stress exerted by trapped lee waves is;

$$\tau_S=\pi U_o \frac{K_*(\chi)A(K_*,\chi)\left|\frac{\partial\hat{w}}{\partial z}\right|^2_{K=K_*(\chi),z=0}}{\int_0^\infty \hat{w}(K_*(\chi),\chi,z)^2 dz}\begin{pmatrix}\cos\chi\\ \sin\chi\end{pmatrix}\Delta\Phi \qquad (22)$$

where K_* is the wave number component in the direction of the surface wind. The variable depth two-layer model can be used to obtain approximate eigenfunctions for $\hat{w}$ and these assist the simplification of eqn (22). At each stage, new averaged upper and lower Scorer parameters are calculated as well as the height of the interface above surface, H. This approach requires the specification of the phase difference of the wave across the lower layer. The eigenvalue problem is to solve the wave equation for each layer subject to $\hat{w}(K_*,0)=0$ and with an evanescent solution in the upper layer. Lee wave modes can only exist if $l_2^2<K_*^2<l_1^2$ (where $l_1(H)$ and $l_2(H)$ are the mean Scorer parameter for the lower and upper layers) and under these circumstances solutions will be of the form:

$$\begin{aligned}&\hat{w}_1=Ce^{-m_2H}\sin(m_1z)\\ &\hat{w}_2=C\sin(m_1H)e^{-m_2z}\\ &with\quad m_1^2=l_1^2-K_*^2>0\\ &and\quad m_2^2=K_*^2-l_2^2>0\end{aligned} \qquad (23)$$

where C is an arbitrary constant and continuity of vertical velocity has been assumed. This would not be true if the basic state wind was discontinuous at the interface but since it is the Scorer parameter which is assumed discontinuous, no inconsistency is implied. Continuity of disturbance pressure and basic state wind across the interface z=H, together with the horizontal momentum equation, implies continuity of horizontal wind perturbation. Furthermore, the continuity equation requires that $\partial\hat{w}/\partial z$ be continuous across the interface which relates m_1 and m_2 by;

$$Tan(m_1H)=-\frac{m_1}{m_2} \qquad (24)$$

From equations (23) and after some manipulation the following equation is satisfied at resonance,

$$\frac{\alpha_L(\ l^2{}_1(H)-l^2{}_2(H)\ )^{0.5}.H_L}{(1+\alpha_L{}^2)^{0.5}.\tan^{-1}(\alpha_L)}+1=0 \qquad (25)$$

where $\tan^{-1}(\alpha_L) = m_1 H$ is a tunable phase difference across the lower layer lying between the limits of $\pi/2$ and π.

If the function on the lhs of eqn(25) changes sign when computed on successive model layers, then a *trapped lee wave* is diagnosed, and an *additional* surface lee wave stress is calculated using equations

$$\frac{1}{XY}\int_{-\infty}^{\infty}\int_{-\infty}^{\infty}\begin{pmatrix}uw\\vw\end{pmatrix}dxdy = \frac{2\alpha_L{}^2\gamma^3\pi K_*A(K_*,\chi)\Delta\phi}{H_L^3(\gamma-1)}U_\tau^2\begin{pmatrix}\cos\chi\\\sin\chi\end{pmatrix} \qquad (26a)$$

with

$$K_*A(K_*,\chi)=\frac{3}{4\pi}\frac{K_{lee}}{K_*^{3/2}}\left((4\cos^2\chi-1)\sigma_{xx}^2+(8\cos\chi\sin\chi)\sigma_{xy}^2+(4\sin^2\chi-1)\sigma_{yy}^2\right) \qquad (26b)$$

where

$$K_{lee}=\frac{1}{K_u^{3/2}-K_l^{3/2}}\ ,\quad K_*^2=\frac{(l_1^2+\alpha_L^2 l_2^2)}{(\alpha_L^2+1)}\ ,\quad \gamma=\Delta\phi/\alpha_L \qquad (26c)$$

and $\Delta\phi \cong 1°$ is the maximum angular width of a lee wave train.

Note that the *trapped lee wave* surface stress is parallel to the surface wind and its magnitude depends on the orographic variance at the resonant wavenumber in the spectrum function, K_*.

Tests have been performed with radiosonde data from 4 stations on the two layer model with good results when phase difference was set to 0.6π implying a peak wave amplitude at z=

5H/6. Heights of wave amplitude maxima and the solutions to the wave equation were compared against a direct numerical solution of the initial structure equation.

Since the horizontal group speed of lee waves is about half the mean flow it takes about 5 hours to set up a 100km lee wave train and in this time it might be assumed that boundary layer dissipation has damped the wave and spread any drag. Bretherton (1969) supposed that turbulence within thin layers might dissipate lee wave energy. Synoptic changes might allow some waves to leak vertically, further downstream. Generally wave/mean flow interaction requires that there be some transient dissipation before the basic flow is forced by the waves.

Although the cause of lee wave dissipation is uncertain, Bretherton showed that an infinite trapped lee wave train has a characteristic vertical momentum flux profile when integrated from far upstream to a point far downstream. From this general momentum flux profile the momentum flux at the two-layer model interface height, H_L, is calculated. For expediency it is assumed that the trapped lee wave stress decreases linearly between the surface and the layer interface. The remaining momentum is deposited linearly between the interface and the top the upper layer. The stress at the interface height is given by,

$$\frac{\overline{uw}(z=H_L)}{\overline{uw}(z=0)} = \frac{\alpha_L^2 l_2^2}{(l_1^2+\alpha_L^2 l_2^2)(M.H_L+1)} \quad \textit{where} \quad M^2 = \frac{(l_1^2-l_2^2)}{(\alpha_L^2+1)} \tag{27}$$

Scorer parameters l^2_1 and l^2_2 are used to calculate the transmission coefficient of long hydrostatic waves. Assuming no downward component of energy flux in the upper layer, the transmission coefficient is given by;

$$T = \frac{2l_1 l_2}{l^2_1+l^2_2+(l^2_1-l^2_2)\cos 2l_1 H} \tag{28}$$

Typically T is between 0.8 and 1.0.

3. VALIDATION AGAINST PYREX DATA

The PYREX program (Bougeault et al. 1990) was a field study over a large area encompassing the Pyrenees mountains, and with the primary aim of diagnosing the momentum budget. Lott and Miller (1995) describe the use of PYREX data to validate a revised parametrization of gravity wave drag recently incorporated into the ECMWF model. Here a different approach is taken to validate the scheme described above.

Broad (1995) uses a 3-dimensional non-hydrostatic mesoscale model with a resolution of 1.5km to simulate the flow over the Pyrenees during IOP3 of PYREX, from 1800 GMT on 14/10/90 to 1200 GMT on 15/10/90. During this period a southerly wind generated large amplitude lee waves, both trapped and vertically-propagating, hydrostatic waves. Three integrations of the model were carried out, each of 4 hours in length. Initial conditions for each experiment were taken from three sequential radiosonde ascents at 0119, 0536 and 1139 GMT (here referred to as 00Z, 06Z and 12Z ascents). The southern boundary of the model was kept at these initial conditions providing a constant inflow upstream of the mountains. The model was found to be able to capture many of the features of the wave motion generated over the Pyrenees during this period.

The vertical profile of momentum flux derived from these simulations are compared here with flux profiles predicted by the parametrization in a single column model (representing a single grid-point of a GCM) initialised with the same wind and temperature profiles used in the mesoscale model experiment. This approach has also been used by Kim and Arakawa (1995) who used a 2-dimensional mesoscale model to test several GWD parameterizations used in GCMs and demonstrated that they fail to provide sufficient low level drag.

Here comparison is made between the flux profiles predicted by the parametrization discussed above and the gravity wave drag scheme of Palmer et al (1986) with the momentum flux profiles diagnosed from the mesoscale model. The gravity wave drag coefficient in the Palmer scheme is $2.5 \times 10^{-5} m^{-1}$, which according to linear theory corresponds to a horizontal wave length of 250km for sinusoidal orography. As sub-grid scale orography corresponds to scales between 20 and 200km it is clear that the value of this coefficient is smaller than that

suggested by direct application of linear theory. In the case of the scheme presented here the value of the coefficient defined in eqn (17) is set to 0.83×10^{-4} (m) corresponding to a range of wave lengths approximately between 30 and 600km, while the lee wave coefficient (K_{lee}, eqn (26c)) is 1.8×10^{5} ($m^{-3/2}$). The value of α is set to 0.4 and β to unity and it is assumed that 2/3 of the surface stress in the high drag state is deposited below the top height of the hydraulic jump layer.

The mesoscale simulations shows a sharp linear decrease of meridional momentum flux below 5km with a more gradual reduction above (figure 1). This behaviour is not reproduced by the Palmer et al (1986) scheme which gives a constant flux through the troposphere with some wave breaking occurring in the lower stratosphere. With the coefficient used here the magnitude of the flux in the lower troposphere is also smaller than that in the mesoscale model. In the case of the 12Z ascent the scheme fails to generate any gravity wave stress as levels used to estimate the stability of the atmosphere (model levels 2 and 3) are neutrally stratified.

The scheme presented above agrees well with the mesoscale model for the 00Z and 06Z case, both in the magnitude of the stress and its vertical distribution. The scheme predicts the flow is in a high drag regime, with the top of the hydraulic jump layer being near 7km. In the 12Z case, unlike the Palmer et al (1986) scheme, the new scheme predicts some gravity wave activity but its magnitude is significantly underestimated and it shows none of the characteristics of the vertical profile of momentum flux diagnosed from the mesoscale model. Again this is due to near neutrality over the model layers which are used to estimate the flow characteristics for the calculation of surface stress. This implies that further thought must be given as to which levels are chosen to estimate the generation of gravity waves. Broad (1995) suggests that the wave activity within the mesoscale model for this case is caused by the undulating surface at the top of the neutral boundary layer where the stably stratified free atmosphere begins.

The gravity waves as simulated by the mesoscale model of Broad (1995) are characterised as partially trapped lee waves. Although the new gravity wave drag scheme predicts low-level wave breaking it does so through the hydraulic jump part of the parametrization, not the

trapped lee waves parametrization. Increasing the value of α to 0.5 moves the flow out of the high drag state in to that associated with long non-hydrostatic waves. The surface stress value is unchanged but no significant drag due to saturation breaking is seen in the lower troposphere. In this instance a small lee wave surface stress is generated, although its value is an order of magnitude lower than that due to the long hydrostatic waves. This indicates that our idealizations of the wave-breaking process are still over simplified and in need of attention.

4. IMPACT UPON MODEL CLIMATOLOGY

The new GWD parametrization has been incorporated into the UK Met. Office Unified Model, replacing the scheme of Palmer et al (1986). Milton and Wilson (1995) discuss the impact of the scheme, together with a parametrization of orographic form drag, upon the performance of the global forecast version of the Unified Model. Here the characteristics of gravity wave activity generated by the scheme and its impact upon the climatology of the climate version of the Unified Model are discussed. The configuration of the model used is that of HADCM2a (the "2nd Climate Version"), being similar to that described by Gregory and Morris (1996) but with a resolution of 2.5x3.75° latitude-longitude with a timestep of 30 minutes. The reader is referred to this paper for further details.

Two 4 year integrations are compared. The first, Sim C, uses the scheme of Palmer et al (1986) to describe gravity wave drag while the second, sim G, incorporates the new gravity wave drag parametrization. The coefficients for each of these schemes are as described in section 2 and 3 above. Gravity wave drag is largest during northern hemisphere winter (December/January/February - DJF) and discussion focuses upon the simulated flow for this season, although brief comments are also made concerning northern hemisphere summer (June/July/August - JJA)

Together with the standard deviation of sub-grid scale orography, several additional surface fields are required by the new parametrization to describe the anisotropy of the sub-grid scale terrain. These are defined by equation (8) but in practice are calculated directly from the US

10' orography data using the formulation of equation (7). The mean gradient of the orography on the model grid is removed during the calculation of the sub-grid standard deviation of orographic height.

Figure 2 shows the surface stress for both simulations for DJF. The horizontal distribution of surface stress over northern continents is similar but elsewhere some differences in details are noted. For example stresses over Greenland, the Sahara and the east African highlands are reduced with the revised scheme. However the most striking difference is the reduction is stress over Antarctica. Here low level flow is along the orography and the revised scheme is able to recognise the anisotropy of the slope. Over Antarctica at 170E, the flow is perpendicular to the mountains and the surface stress generated by the anisotropic scheme is larger than that of the isotropic scheme.

Differences are seen in the vertical distribution of drag predicted by the two schemes. The revised scheme generates less mid-level wave breaking in northern hemisphere mid-latitudes (figure 3) but provides increased drag in the lower troposphere, as indicated by the single column model. However the magnitude of the drag in the upper troposphere is little changed in the zonal mean. Indeed if the zonal mean surface stress from the two experiments is compared (not shown) there is little difference in the magnitude of the stress predicted from both schemes over most latitudes. The fact that both schemes produce very similar amounts of surface stress even though its estimation is different suggests that, at least in climate integrations where the flow has time to reach some equilibrium, the magnitude of the stress is determined not by the constants in the gravity wave drag scheme but by the requirement that the atmosphere has to have a certain level of gravity wave drag stress in order to balance dynamical transports which in the troposphere remain little changed between the two simulations (not shown).

Figure 4 shows the contribution to wave drag from saturation/critical level, hydraulic jump and trapped lee wave breaking mechanisms for sim G. Saturation wave breaking in the upper troposphere of sim G is similar to that of sim C (in which it is the only wave breaking mechanism), as also is the low level drag in the tropics (0-25N) and near 60N, although it is

restricted to below 900mb in sim G rather than 800mb as in sim C[2]. However in the northern mid-latitudes around 45N wave breaking in the lower and mid-troposphere is dominated by the breaking of trapped lee waves (below 900mb) and the hydraulic jump response. The latter process also provides low level drag over Antarctica near 170E.

The spatial distribution of the gravity wave drag in the lower and upper troposphere from the two simulations is illustrated in figure 5 and 6 which shows the acceleration due to gravity wave breaking in levels 4 and 15 of the model respectively (~900 and 100mb for a surface pressure of 1000mb). In the lower troposphere larger drag is found with the new scheme over the Rockies, Europe and Siberia while lower values are seen over Central America and Africa. At upper levels, although zonal-mean cross sections of gravity wave drag for the two simulations are similar, the spatial distribution of the drag is different. With the new scheme, wave breaking is greater over the Rockies, being offset in the zonal mean by the reduced drag over eastern China and Japan. Also upper-level wave breaking is increased over the Himalayas in sim G. With the original gravity wave drag scheme most of the gravity wave stress in this region was deposited in the lower and mid-troposphere.

Originally the introduction of gravity wave drag into GCMs had a large impact upon the simulated mean sea level pressure (p_{msl}) patterns and wind fields. Here, although some aspects of the morphology of the drag have been modified, the net level of the gravity wave stress is approximately the same. Although local patterns may differ with the increased amounts of low level drag, one might not expect the overall pattern of the flow to be as affected as greatly as in earlier studies (for example as in Slingo and Pearson, 1986). Figure 7 shows the p_{msl} patterns for DJF from simulations C and G (4 year means) together with a climatology derived from ECMWF analyses (from 1987 to 1993). In simulation G, the flow

---

[2]Since this study was performed it has been discovered that in the version of model used stress generated by low level northerly or easterly flow was dissipated in the model level immediately above that in which it was generated. This accounts for the restricted depth of the drag in the tropics of sim G compared to sim C. Subsequent simulations carried out using a revised version of the scheme show a deep layer of low level drag in the tropics. However the seasonal climatology of the model and the distribution of gravity wave drag in the mid-latitudes is unaffected by the change (S.Webster, personal communication) and the results discussed here provide a valid description of the performance of the scheme in climate simulations.

over the United Kingdom is more westerly, with the north Atlantic trough extending further eastward between Iceland and Scandinavia. The strength of the flow over Russia is stronger with the new gravity wave drag scheme, but is too southerly due to the failure of the Siberian high to build to the observed magnitude over central Asia. Over north America the flow is less zonal, in better agreement with observations. The largest changes in p_{msl} are found in the Antarctica circumpolar trough. In simulation C the 984mb contour was continuous around the globe, whereas this is broken into several distinct regions in simulation G, being closer to the observed fields, although still too deep. This appears to be a consequence of the removal of stress along the edge of Antarctica through the use of anisotropic orography.

Figure 8 shows the zonal mean difference of zonal wind from simulations C and G from a climatology of ECMWF analyses (1987 to 1993) for DJF. In the northern mid-latitudes wind errors are slightly reduced, due to the reduction of the area within the north Atlantic jet greater than $40ms^{-1}$ being reduced. However in the tropics near 15N, low level wind errors are increased associated with a stronger easterly flow over Africa due to the reductions in gravity wave stress noted earlier. Wind errors are also increased in the vicinity of Antarctica due to the reduction of gravity wave drag in this region.

Considering northern summer (June/July/August - JJA), gravity wave drag stress is much smaller than for DJF in many regions (for example over the Rockies) (figure 9). As in DJF, large stresses predicted over Antarctica by the original gravity wave drag scheme (sim C) are reduced through the introduction of anisotropic orography. Changes in flow on introduction of the new scheme are small, although the maximum zonal mean wind error in the northern hemisphere is shifted poleward. This comes about through a reduction in the speed of the upper tropospheric zonal wind over the north Atlantic, north America and north Pacific. Being mainly over the ocean this is obviously not a direct consequence of the new scheme but is perhaps linked to the general adjustment of the large-scale flow to changes in the distribution of gravity wave drag.

5. INFLUENCE OF FORM DRAG UPON GRAVITY WAVE DRAG STRESS

Several other processes other than gravity waves can exert drag upon the atmospheric flow in mountainous regions. Smith and Jackson (1996) describe a parametrization which represents the pressure force associated with enhanced turbulent dissipation in mountainous regions. This parametrization is based upon the work of Mason (1985). The pressure force on a hill (F_p) in neutral conditions can be expressed by the aerodynamic formula

$$F_P=\tau_* S=\frac{1}{2}C_D^{OROG}AU^2(Z_H) \tag{29}$$

where C_D^{OROG} is an orographic drag coefficient (currently 0.3), A is the frontal area of the obstacle, and U is the wind speed defined at a height z_H, τ_* the surface stress associated with the pressure force and S a horizontal area.

The use of effective roughness lengths to parametrize the form drag is prompted by modelling studies (Wood and Mason,1993). Observations in hilly terrain (Grant and Mason,1990) show that the areally averaged flow sufficiently far above the surface behaves logarithmically even over large roughness elements such as hills. The areally averaged 'effective' surface stress is linked to an 'effective' roughness length, z_{om}^{eff}, representing the combined effects of all roughness elements within a grid box. The model wind at a height z_h is given by

$$\bar{U}(z_h)=\frac{u_*^{eff}}{k}\ln\left(\frac{z_h}{z_{om}^{eff}}\right) \tag{30}$$

where k is von Karmans constant.

The height at which this analysis is valid is z_h taken to be half the peak to trough height of the sub-grid scale orography. The effective roughness length itself is determined by averaging the expressions for the stress due to unresolved form drag and the shear stresses to give

$$\frac{k^2}{\left[\ln\left(\frac{z_h}{z_{om}^{eff}}\right)\right]^2}=\frac{1}{2}C_D^{OROG}\frac{A}{S}f_D(Ri)+\frac{k^2}{\left[\ln\left(\frac{z_h}{z_{om}}\right)\right]^2} \tag{31}$$

where z_{om} is the prescribed roughness length for momentum derived from vegetative effects. The term f_D is a stability factor dependant on the local Richardson number (Ri) set to 1 when Ri<0 and reducing linearly to zero as Ri increases to 1, thus tailing off form drag in stable conditions. The frontal (silhouette) area of unresolved orography per unit area, A/S needs to be calculated from high resolution data sets. A 30" resolution data set for Europe has been used to derive A/S for this region and a linear regression is performed relating global US Navy 10' standard deviations to the grid-box average A/S for the European region. This regression was then used to estimate global values for z_h. A/S is not allowed to exceed 0.2 and the maximum value of z_h is 1km.

A further 4 year integration was carried out (simulation GR), parallel to simulation G but also including the orographic roughness parametrization described above. The gravity wave drag scheme used in both of these experiments is identical in formulation. Figure 11 shows the zonal mean stress (averaged over land) for sim G and simulation GR for DJF (4 year mean). In northern mid-latitudes the net stress due to gravity wave drag and turbulence is roughly constant in both simulations. However the contribution of the gravity wave drag and boundary layer schemes to the net stress is different. In sim G between 30 and 60N, gravity wave drag stress is larger than that for the boundary layer scheme but in sim GR, the magnitudes of the two stresses are roughly equal. Reduction in gravity wave stress comes about through a reduction in low level wind speed over land. The reduction is gravity wave drag is seen in figure 12c, with zonal mean accelerations due to gravity wave breaking being approximately half those found in sim G (fig. 3b). Drag due to boundary layer processes has increased in the upper part of the boundary layer with the use of larger roughness lengths for momentum (fig. 12(a) and (b)).

Introduction of orographic roughness has a positive impact upon the circulation pattern of the northern hemisphere during DJF as illustrated by the p_{msl} pattern (figure 13). The surface flow over north America becomes less zonal, while the north Atlantic trough is less deep. The Siberian anticyclone is better positioned, with the area with pressures above 1028mb being more coherent than in previous integrations. The flow over Scandinavia and northern Russia is also better simulated. However, while errors in the strength of the lower troposphere zonal mean flow are reduced through the introduction of increased low level drag

(figure 14), errors in the upper level flow around 45N are increased due to the reduction of the magnitude of the drag due to gravity wave breaking. However the wind structure in the lower stratosphere appears improved with the reduction in gravity wave drag as illustrated by figure 15.

Figure 15(b) and (c) shows zonal mean wind for sim G and sim GR together with the regions of positive drag due to gravity wave breaking superimposed. A log pressure vertical co-ordinate has been used to enable the impact of gravity wave drag in the upper troposphere and lower stratosphere to be seen. Also shown is a climatology of zonal mean wind derived from ECMWF analyses (fig 15(a)). As noted previously a reduction in gravity wave drag in the vicinity of the northern hemisphere jet is seen. The level of maximum drag due to wave breaking is lifted, from 100mb in sim G to just below 50mb in sim GR, drag increasing in the stratosphere. A similar effect is seen in the southern hemisphere jet although levels of gravity wave drag are much smaller there. These changes are caused by the smaller magnitude of the gravity wave stress propagating upwards from the surface. Wave breaking in the upper troposphere and lower stratosphere is by saturation effects and critical level absorption. With the former, assuming changes to the wind profile are small, smaller values of gravity wave surface stress may propagate higher before they reach saturation. Above 100mb the reduction in gravity wave drag appears to have a beneficial impact upon the flow. In sim G the $15ms^{-1}$ contour around the northern hemisphere jet is closed whereas the climatology indicates that it remains open. Below 50mb the structure of the wind in simulation GR in the upper part of the northern hemisphere jet is in better agreement with the climatology, with the $15ms^{-1}$ contour remaining unclosed around the jet. Above 50mb the simulation of the stratospheric flow remains poor, with the level of maximum winds at the top of the model being located to close to the equator.

6. SUMMARY

A new gravity wave drag scheme, incorporating anisotropic orography, low level wave breaking associated with trapped lee waves and hydraulic jump phenomena and flow blocking, has been described. The scheme is based upon simple models of the generation/breaking of

atmospheric gravity waves and on idealised specifications of the orography. The performance of the scheme has been compared to explicit simulations of gravity waves over the Pyrenees using a high resolution non-hydrostatic mesoscale model and provides a better representation of the effects of gravity wave breaking that the previous scheme used in Met. Office models (Palmer et al, 1986) with greater drag in low levels. It should be noted that the schemes parameters were chosen on the basis of theoretical arguments and observations, rather by tuning to obtain a realistic result. In this regard the scheme is an improvement on that of Palmer et al (1986) in which the gravity wave surface stress coefficient had to be set at too low a value (compared to linear theory) in order to obtain a reasonable amount of stress.

Inclusion of the new scheme into the Met. Office Unified Model has rather a neutral impact upon the model climate despite significant changes in the vertical distribution of wave drag. Changes in simulated circulation are not well correlated to the changed drag distribution, in contrast to results reported by Milton and Wilson (1996) who studied the impact of the revised gravity wave drag and orographic roughness scheme upon short range forecasts produced by the global forecast version of Unified Model (with a resolution of 0.83x1.25° latitude-longitude). This suggests that in the short range (out to a few days of model integration) the response of the flow to a change in momentum forcing is approximately linear. However on seasonal timescale the changes in the large-scale flow seen on the introduction of the new gravity wave drag scheme reflect the flow configuration required by dynamical processes to balance the orographic induced drag. Gregory et al (1996), discussing the impact of the convective momentum transports upon the climatology of the Unified Model, shows that on the seasonal timescale the tendencies due to dynamical and physical processes are approximately in balance.

Introduction of a parametrization of orographic form drag, represented by an enhanced roughness length in the presence of orography, improves the simulated flow at low levels but causes the magnitude of gravity wave stress to be halved. However the net surface stress produced by the two scheme remains approximately constant at most latitudes. This is similar to the results presented by Slingo and Pearson (1986) who considered the introduction of gravity wave drag into the 11-layer UK Met. Office Climate Model. They found that the total stress due to mountain torque and physical processes was similar in experiments with and

without gravity wave drag. Introduction of gravity wave drag brought about a reduction in the frictional stress due to boundary layer processes. In both their experiments the mountain pressure torque was similar. This again illustrates that in climate simulations the magnitude of the stress due to orography adjusts to that required to balance the transport of momentum by the large-scale flow.

Although gravity wave drag was introduced into GCMs to control excessive westerly flow, a reduction of the magnitude found with the introduction of orographic roughness does not degrade the simulated flow greatly. Although systematic errors in the zonal mean wind increase in the vicinity of the core of the mid-latitude jet during northern winter, positive speed errors over northern mid-latitudes at low levels are reduced, as are wind errors in the lower stratosphere. Other physical mechanisms also provide a drag on the flow in the upper troposphere. Convective momentum transports (Gregory et al, 1996) provide a deceleration of around $0.5ms^{-1}day^{-1}$ at the jet core level which alleviates one third of the bias seen in figure 14 near 150mb at 45N during DJF. It may be that too much reliance has been placed upon orographic gravity waves to provide damping on the upper level flow of the mid-latitudes. Other sources of gravity waves (such as deep convection penetrating through the tropopause) may also play a role in providing a source of gravity wave activity and drag in the stratosphere. This may be of importance in regions where there is little orography, such as the southern hemisphere where systematic errors in the wind field remain large.

Further refinements could be made to the schemes described here, especially to the theoretical formulation of that part of the scheme which produces low level wave breaking (trapped lee waves and hydraulic jumps). The scheme currently assumes that the direction of the stress vector is constant with height in the direction of the near surface generating wind. Recent work by Shutts (1995) and Broad (1995) has shown that an ensemble of orographic waves generated by anisotropic orography has a continuum of critical levels as the wind turns with height. This would presumably distribute the gravity wave drag over broader layers of the atmosphere. The sensitivity of gravity wave stress to boundary layer processes may be reduced if the levels used to estimate the near surface gravity wave stress were taken to be just above the boundary layer. The specification of the orographic roughness length is also crude at the present time. Further refinements will have to wait until global orographic data

sets are available with a resolution of around 1km.

8. ACKNOWLEDGEMENTS

The authors would like to thank A.Broad for supplying profiles of gravity wave drag stress from mesoscale model simulations of PYREX observation periods. Our thanks also to R.N.B.Smith and S.Jackson for making the orographic roughness parametrization available.

9. References

Bretherton, F.P (1969) 'Momentum transport by gravity waves' Quart. J. Roy. Met. Soc., 95, 213-243

Bannon, P.R. and Yukas, J.A., 1990 : On mountain drag over complex terrain., Meteorol. Atmos. Phys., **43**, 155-162

Bougeault, P., Jansa Clar, A., Benech, B., Carrissimo, B., Pelon, J. and Richard, E., 1990 : Momentum budget over the Pyrenees: The PYREX experiment., Bull. Am. Meteorol. Soc., **71**, 806-818

Broad, A.S., 1995 : Linear theory of momentum fluxes in 3-D flows with turning of the mean wind with height., Q.J.R. Meteorol. Soc, **121**, 1891-1902

Broad, A.S., 1996 : High resolution numerical model integrations to validate gravity wave drag parametrization schemes:- A case study., Submitted to Quart. J. Roy., Meteor. Soc.

Gregory, D., Kershaw, R. and Inness, P.M., 1996 : Parametrization of momentum transports by convection. II : Tests in single column and general circulation models., Submitted for publication in Quart. J. Roy. Meteor. Soc.

Gregory, D. and Morris, D., 1996 : The sensitivity of climate simulations to the specification of mixed phase clouds., Accpted for publication in Climate Dynamics.

Grant, A.L.M. and Mason, P.J., 1990 : Observations of boundary-layer structure over complex terrain., Quart. J. Roy. Meteor. Soc., **116**, 159-186

Kim, Y.-J. and Arakawa, 1995 : Improvement of orographic gravity wave parametrization using a mesoscale gravity wave model., Accepted for publication in J. Atmos. Sci.

Lott, F. and Miller, M., 1996 : A new sub-grid scale orography drag parametrization: its formulation and testing., Submitted to Q.J.R. Meteorol. Soc.

Mason, P.J., 1985 : On the parametrization of orographic drag, ECMWF seminar proceedings on "Physical Parametrization of numerical models of the atmosphere", 9-13 Sept 1995, Shinfield Park, Reading, U.K.

Milton, S.F. and Wilson, C.A., 1995 : The impact of parametrized subgridscale orographic forcing on systematic errors in a global NWP model., Accepted for publication in Mon. Wea. Rev.

Palmer, T.N., Shutts, G.J. and Swinbank, R., 1986 : Alleviation of systematic westerly bias in general circulation and numerical weather prediction models through an orographic gravity wave drag parametrization., Quart. J. Roy. Met. Soc., **122**, 2056-2066

Peltier, W.L. and Clark, T.L., 1979 : The evolution and stability of finite amplitude mountain waves. Part II : Surface wave drag and severe downslope windstorms., J. Atmos. Sci., **36**, 1489-1529

Rottman, J.W. and R.B. Smith (1989) 'A laboratory model of severe downslope winds' Tellus, 41A, 401-415.

Shutts, G.J., 1990 : A new Gravity Wave Drag Parametrization Scheme for the Unified Model. Turbulence and Diffusion Note 2, Available from APR-Div, Meteorological Office, London Road, Bracknell, Berks. RG12 2SX. United Kingdom

Shutts, G.J., 1992 : Observations and numerical simulation of a partially-trapped lee wave over the Welsh mountains., Mon.Wea. Rev., **120**, 2056-2066

Shutts, G.J., 1995 : Gravity wave drag parametrization over complex terrain: The effect of critical-level absorption in directional wind-shear., Q.J.R.Meteorol. Soc., **121**,1005-1021

Shutts, G.J. and Broad, A.S., 1992 : Lee waves over the U.K.: Observations and model simulation., ECMWF Seminar proceedings "Validation of models over Europe, Vol 1", 7-11 Sept 1992, Sinfield Park, Reading, U.K.

Slingo, A. and Pearson, D.W., 1986 : A comparison of the impact of an envelope orography and a parametrization of orograhic gravity-wave drag on model simulations., Q.J.R. Meteorol. Soc., **113**, 847-870

Smith, R.B., 1985 : On servere downslope windstorms., J. Atmos. Sci., **42**, pp2597-2603

Smith, R.N.B. and Jackson, S., 1996 : A parametrization of orographic form drag and its effects in the UK Meteorological Office Unified Model., In preparation

Wood, N. and Mason, P.J., 1993 : The pressure force induced by neutral turbulent flow over hills., Q.J.R. Meteorl. Soc., **121**, 433-444

Figures

Figure 1 Profiles of gravity wave stress for (a) 00Z, (b) 06Z and (c) 12Z on 15/10/90 (during PYREX IOP3) predicted by the new gravity wave drag parametrization (solid), the Palmer et al (1986) parametrization (dot dash) and estimated from mesoscale model simulation (long dash). For the 12Z profile the Palmer et al (1986) scheme predicts zero stress.

Figure 2 Distribution of gravity wave surface stress in (a) sim C and (b) sim G for DJF (4 year mean).

Figure 3 Zonal mean gravity wave drag in (a) sim C and (b) sim G for DJF (4 year mean). Contour interval is 1m/s/day.

Figure 4 Contribution of (a) saturation/critical, (b) hydraulic jump and (c) trapped lee wave breaking mechanisms to total zonal mean gravity wave drag for sim G for DJF (4 year mean). Contour interval is 0.5m/s/day.

Figure 5 Distribution of gravity wave drag in level 4 of the model (near 900mb when surface pressure is 1000mb)in (a) sim C and (b) sim G for DJF (4 year mean).

Figure 6 Distribution of gravity wave drag in level 15 of the model (near 100mb when surface pressure is 1000mb) in (a) sim C and (b) sim G for DJF (4 year mean).

Figure 7 Mean sea level pressure during DJF. (a) Climatology (1987-93), (b) sim C and (c) sim G. (b) and (c) are 4 year means.

Figure 8 (a) Zonal mean zonal wind climatology for DJF (1987-93) and difference of simulated wind from the climatology for (b) sim C and (c) sim G (4 year means).

Figure 9 Distribution of gravity wave surface stress in (a) sim C and (b) sim G for JJA (4 year mean).

Figure 10 (a) Zonal mean zonal wind climatology for JJA and difference of simulated wind from the climatology for (b) sim C and (c) sim G (4 year means).

Figure 11 Zonal mean surface stress due to gravity wave drag scheme (solid), boundary layer scheme (long dash) and total surface stress for (a) sim G and (b) sim GR for DJF (4 year mean).

Figure 12 Zonal mean drag due to boundary layer processes in (a) sim G and (b) sim GR and (c) zonal mean gravity wave drag for sim GR for DJF (4 year mean).

Figure 13 Mean sea level pressure for DJF (4 year mean) for sim GR.

Figure 14 Zonal mean difference of zonal mean wind from climatology for DJF (4 year mean) for sim GR.

Figure 15 (a) Zonal mean zonal wind climatology for DJF plotted on a log pressure scale

together with zonal mean zonal wind (contours) and gravity wave drag (shading) for (b) sim G and (c) sim GR for DJF (4 year mean).

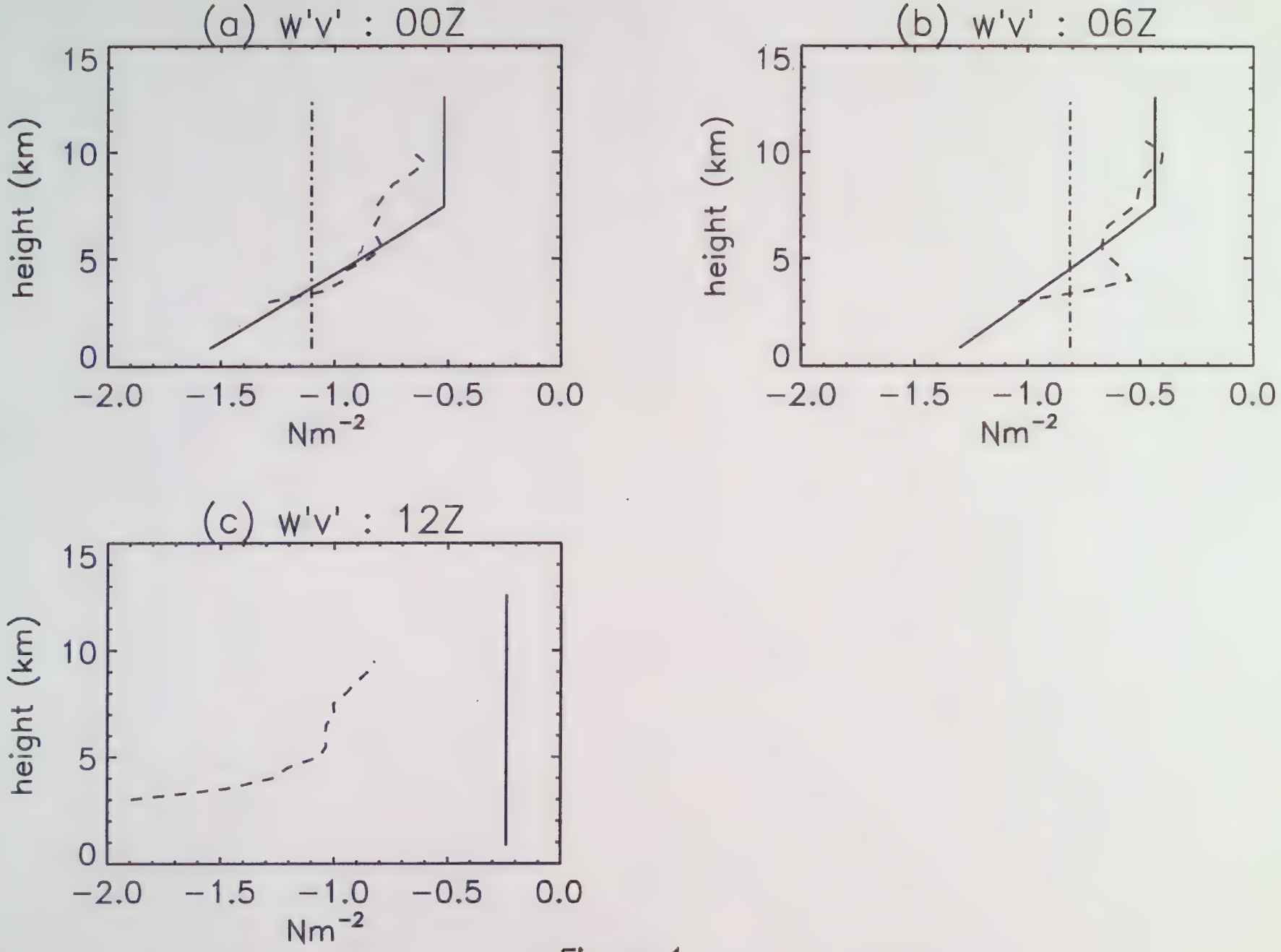

Figure 1

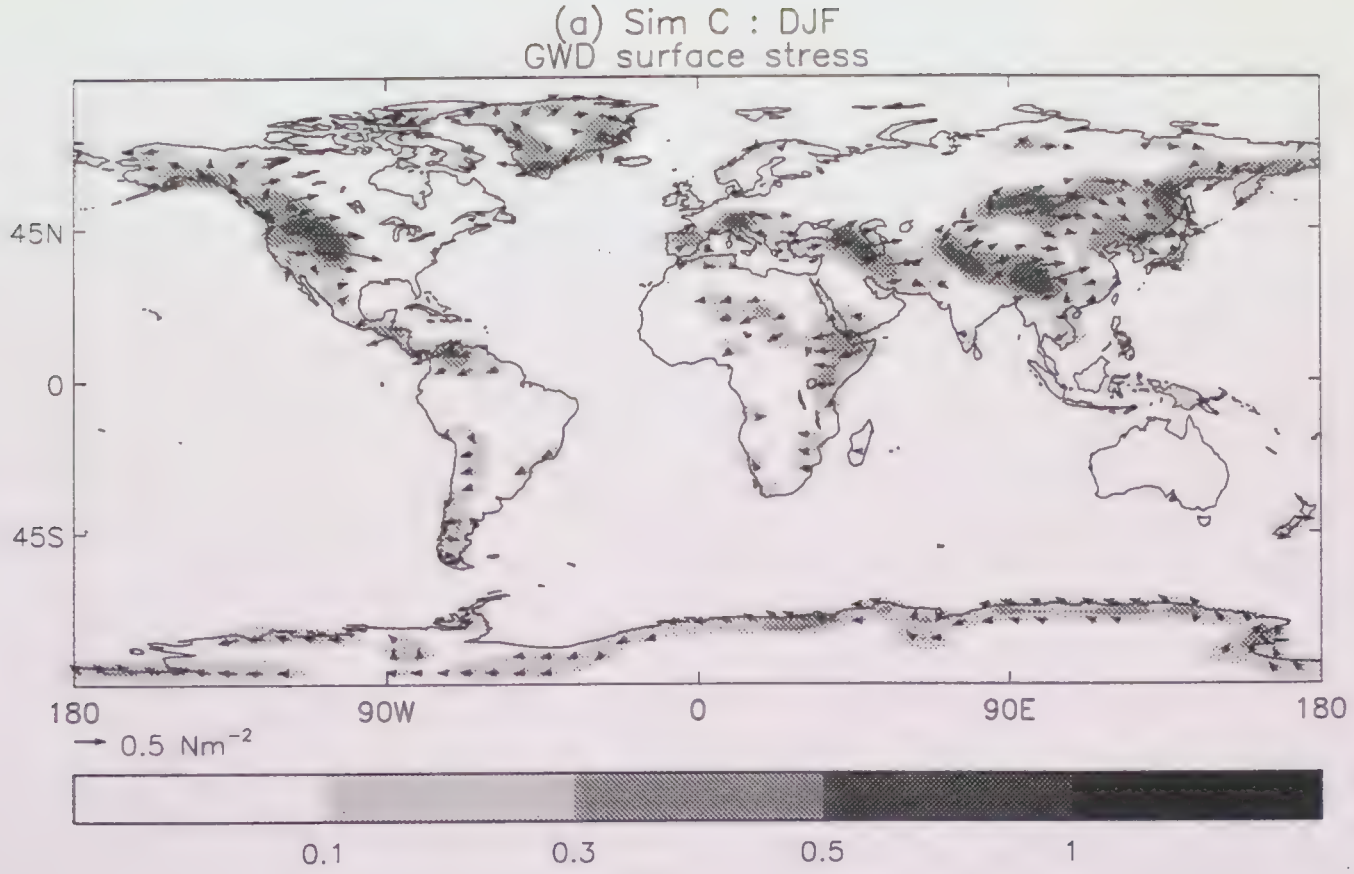
(a) Sim C : DJF
GWD surface stress
45N
0
45S
180
90W
0
90E
180
0.5 Nm^{-2}
0.1
0.3
0.5
1

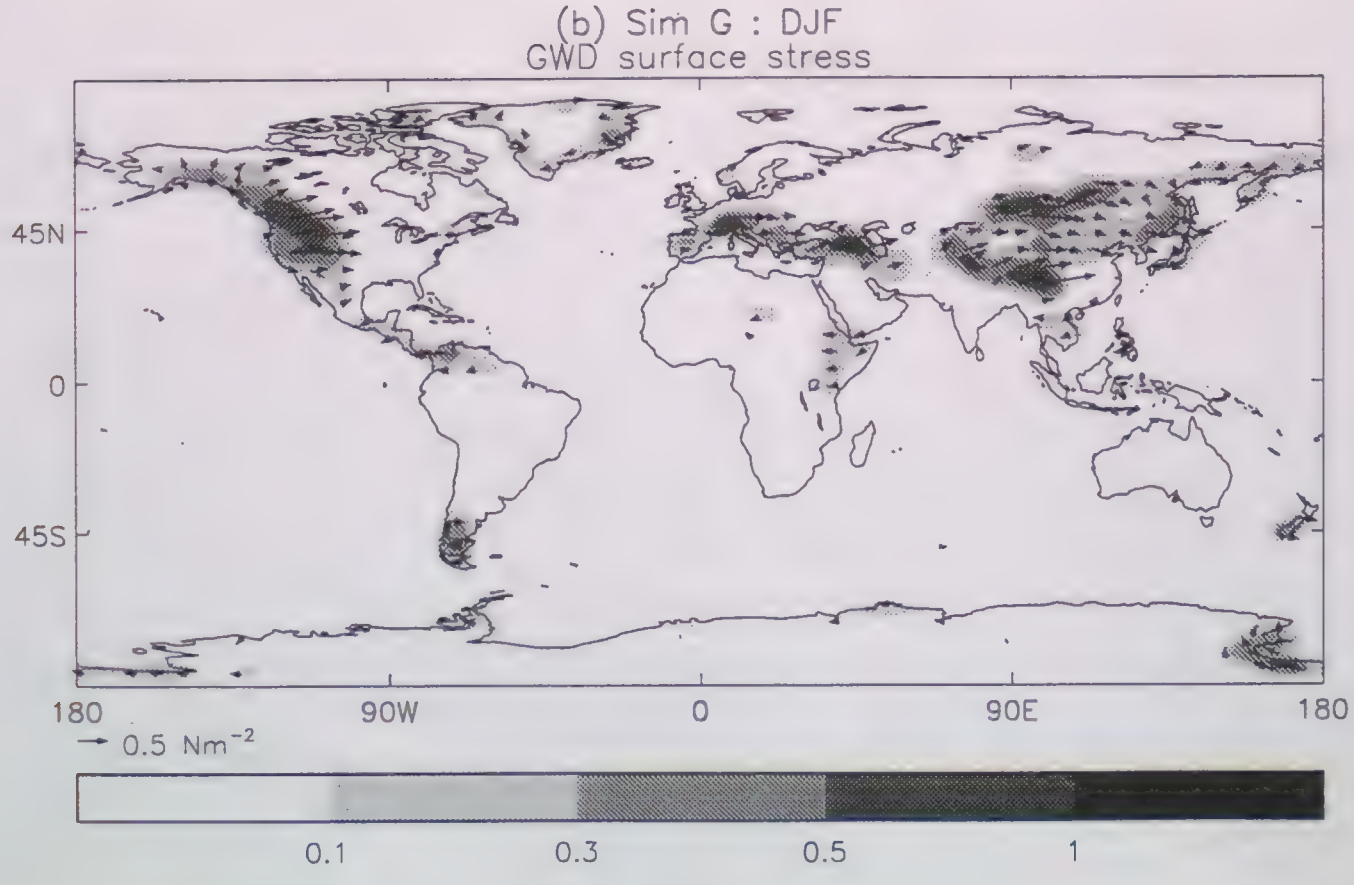
(b) Sim G : DJF
GWD surface stress
45N
0
45S
180
90W
0
90E
180
0.5 Nm^{-2}
0.1
0.3
0.5
1

Figure 2

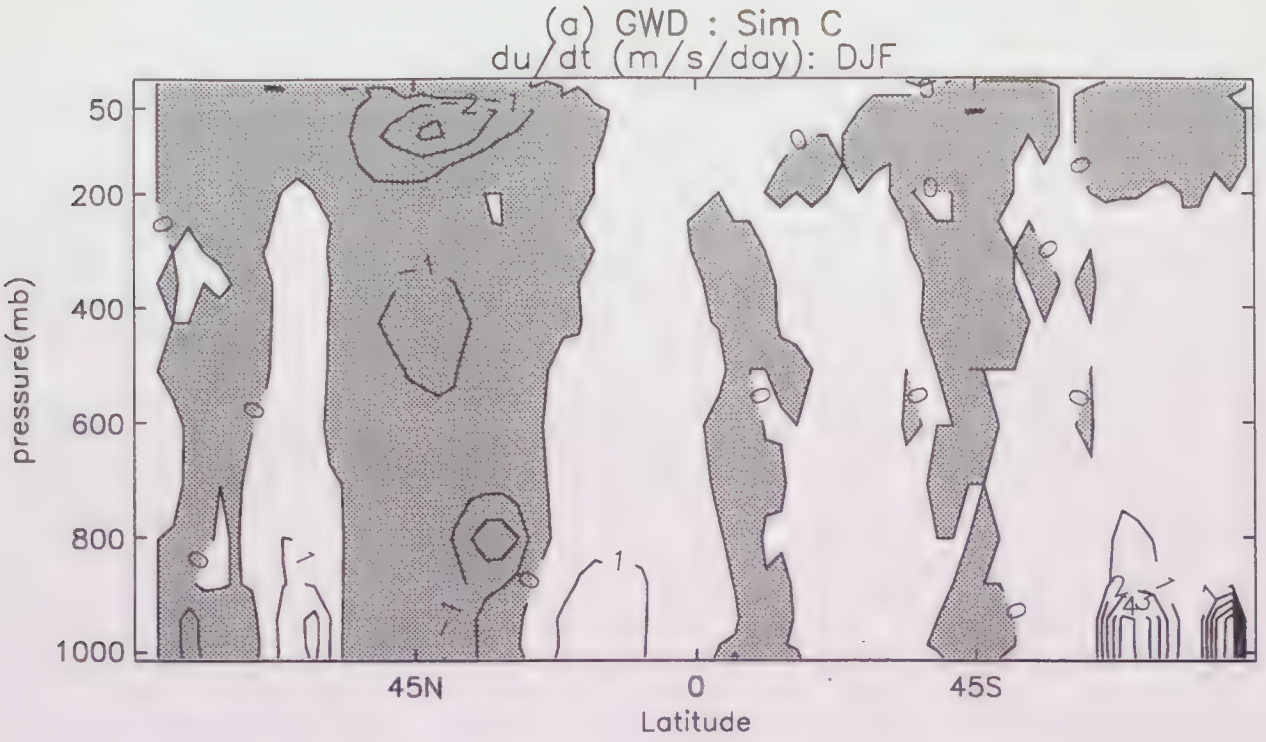
(a) GWD : Sim C
du/dt (m/s/day): DJF
pressure(mb)
50
200
400
600
800
1000
45N
0
45S
Latitude

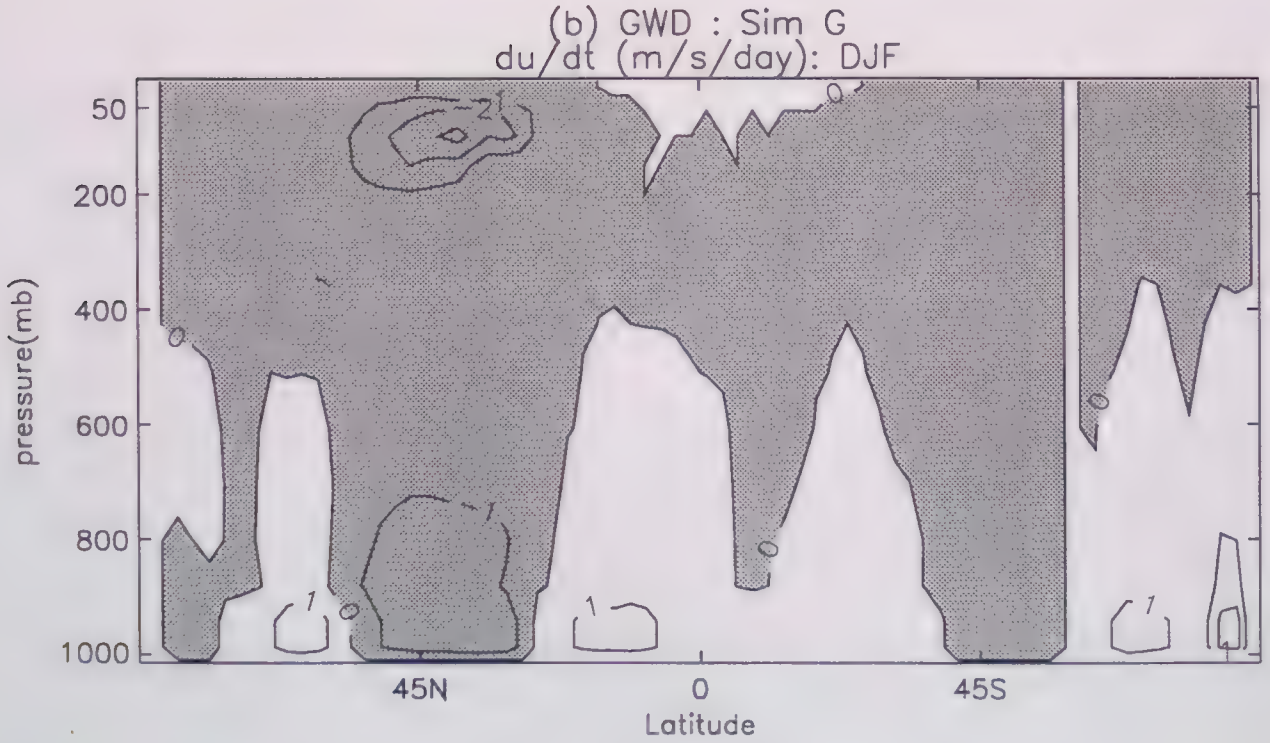
(b) GWD : Sim G
du/dt (m/s/day): DJF
pressure(mb)
50
200
400
600
800
1000
45N
0
45S
Latitude

Figure 3

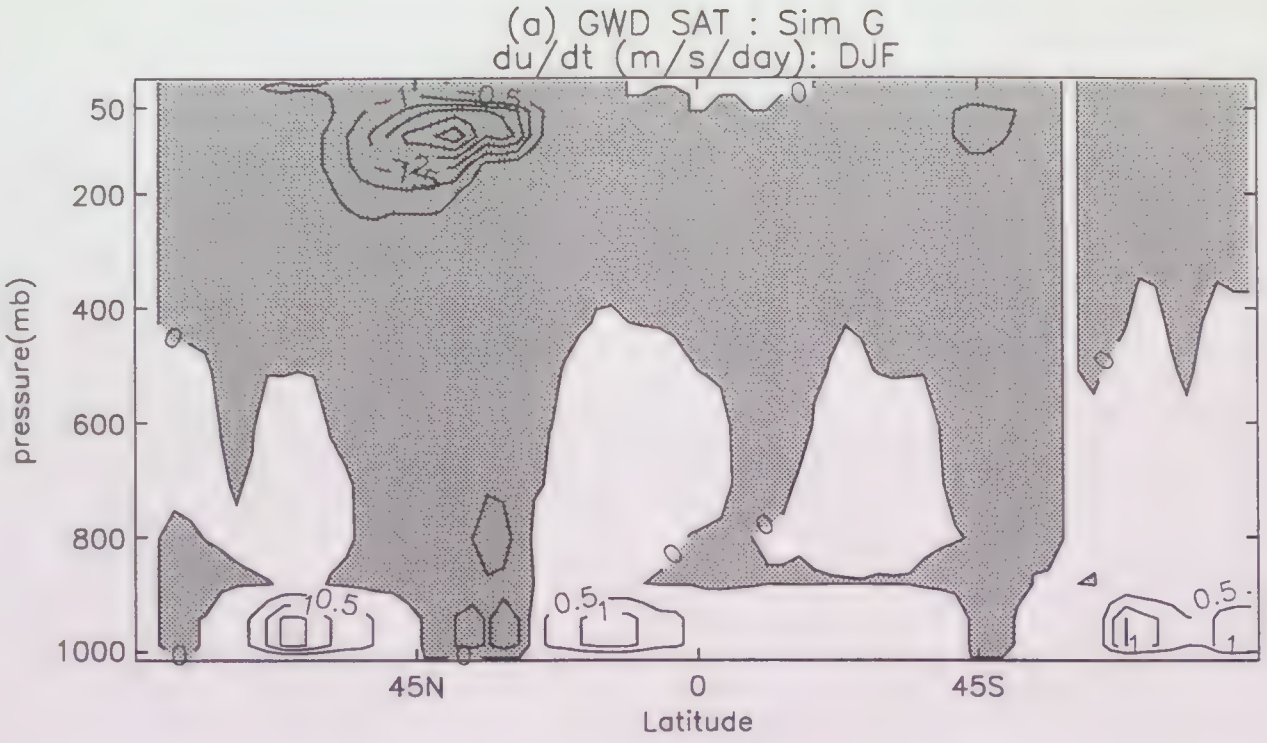
(a) GWD SAT : Sim G
du/dt (m/s/day): DJF
pressure(mb)
50
200
400
600
800
1000
45N
0
45S
Latitude

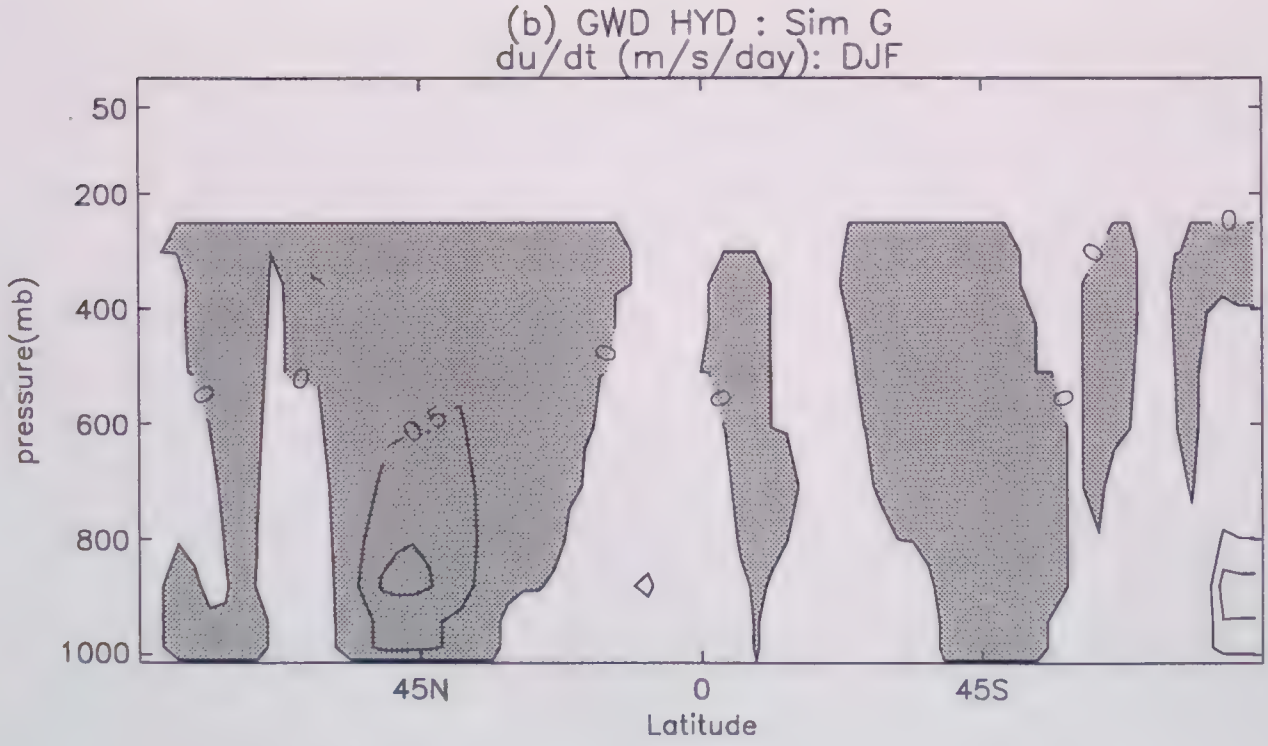
(b) GWD HYD : Sim G
du/dt (m/s/day): DJF
pressure(mb)
50
200
400
600
800
1000
45N
0
45S
Latitude

Figure 4

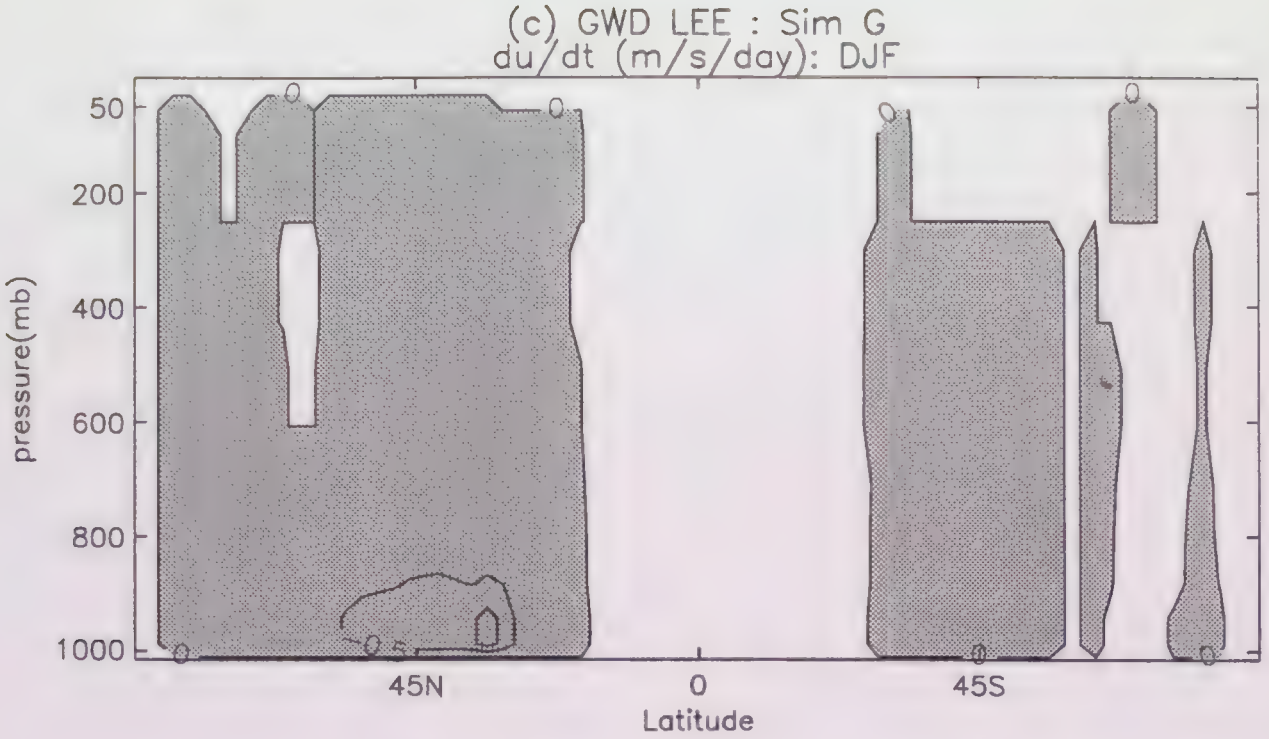

Figure 4 contd

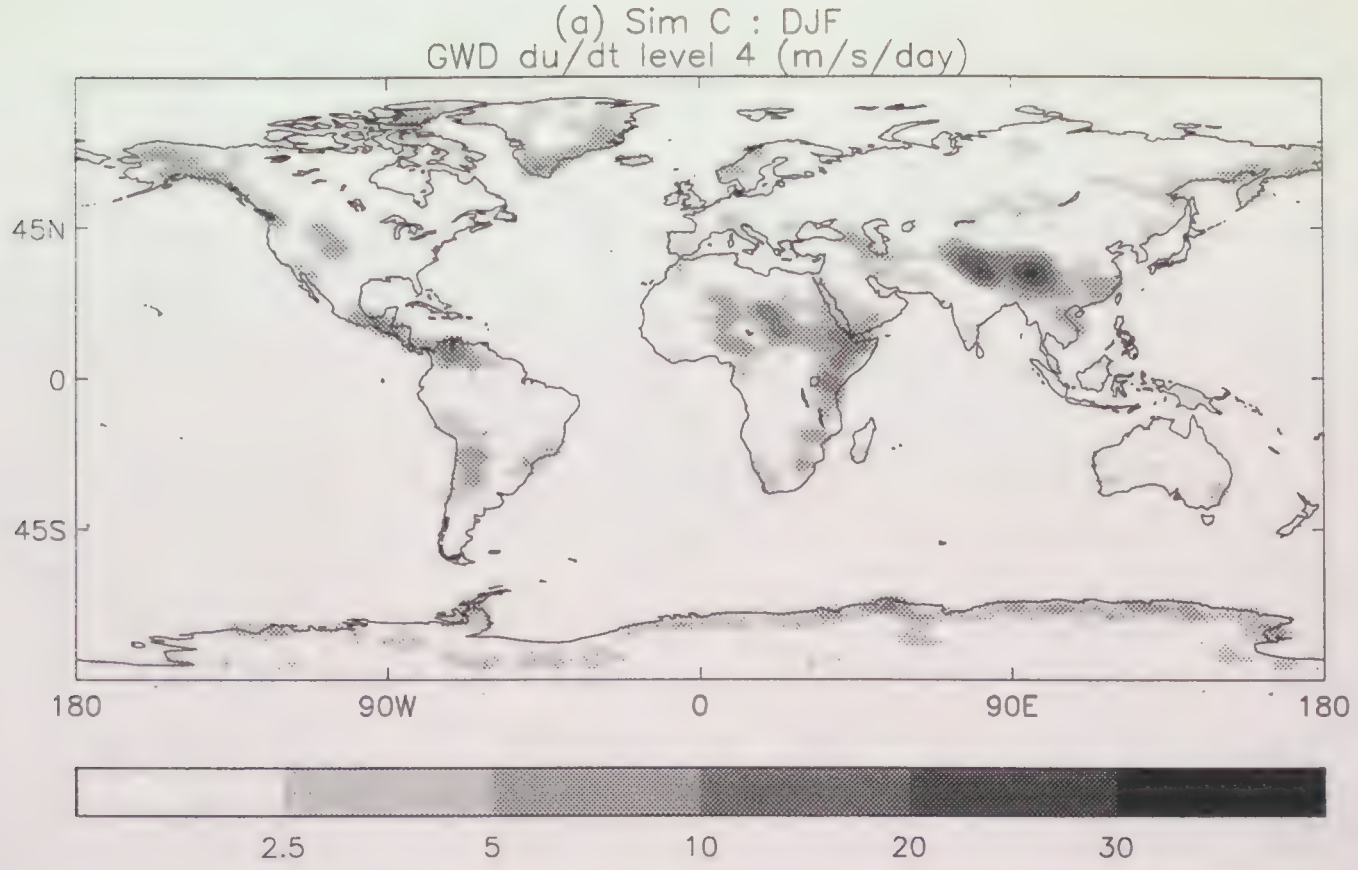
(a) Sim C : DJF
GWD du/dt level 4 (m/s/day)
45N
0
45S
180
90W
0
90E
180
2.5
5
10
20
30

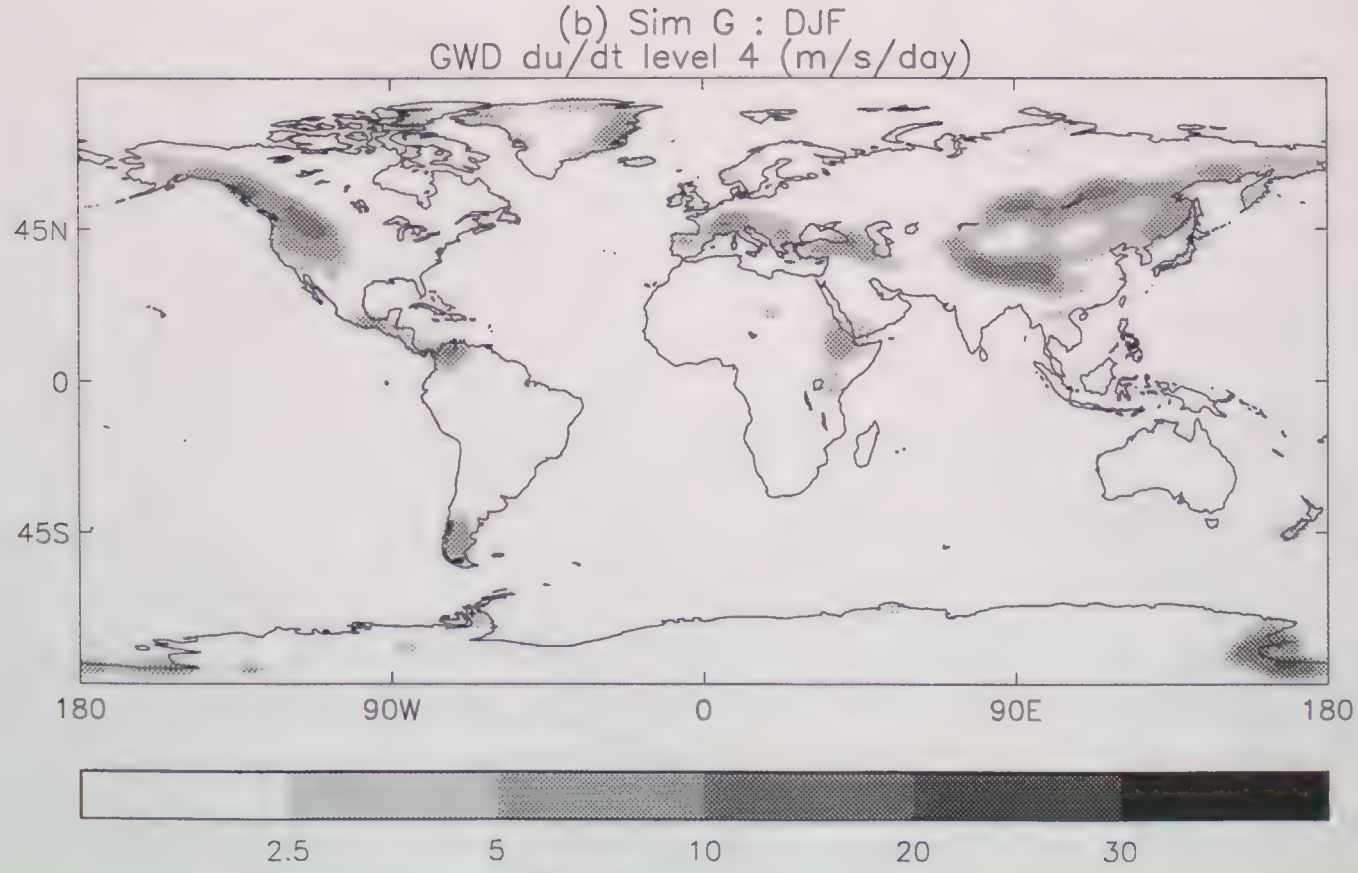
(b) Sim G : DJF
GWD du/dt level 4 (m/s/day)
45N
0
45S
180
90W
0
90E
180
2.5
5
10
20
30

Figure 5

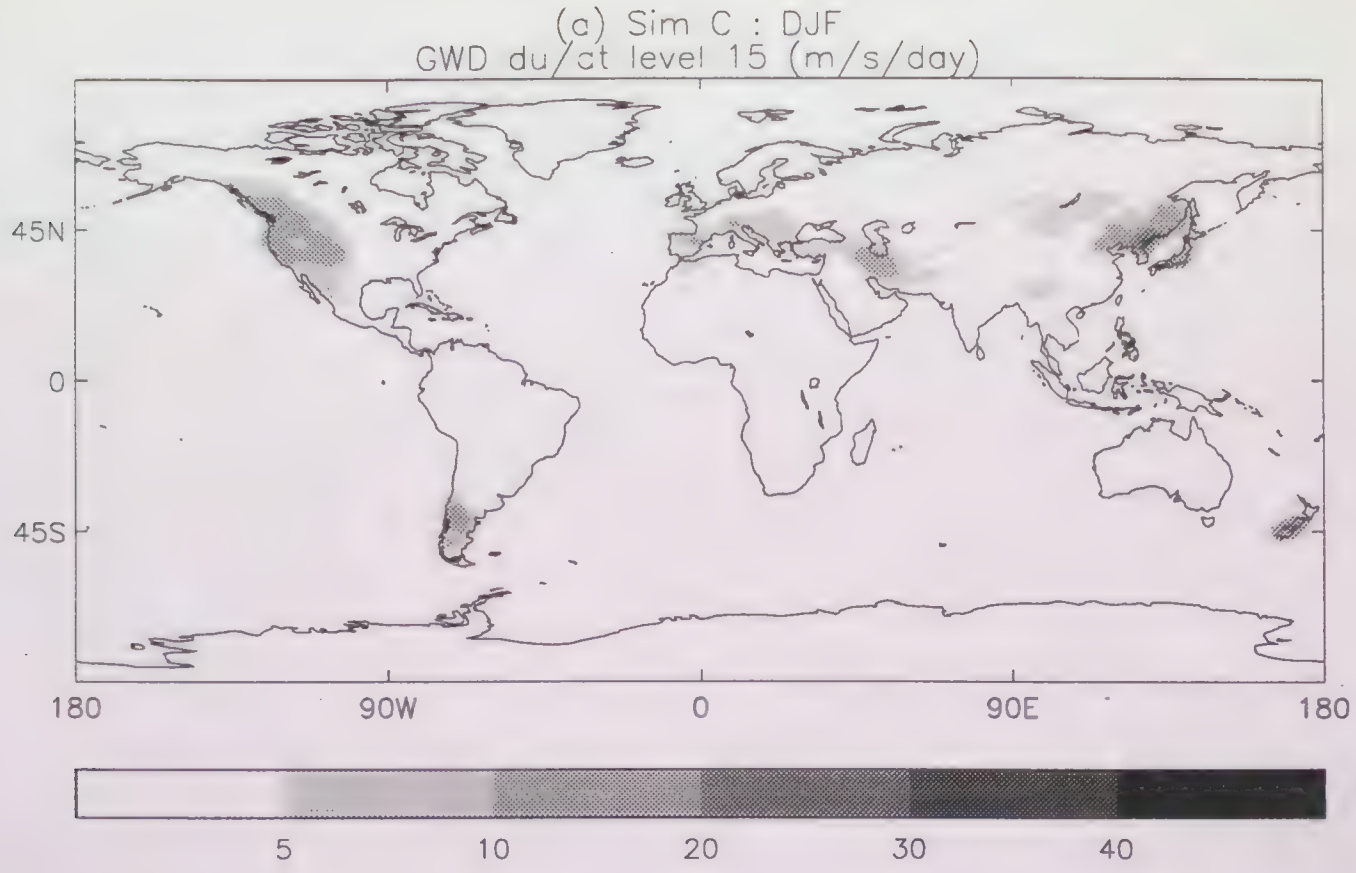
(a) Sim C : DJF
GWD du/dt level 15 (m/s/day)
45N
0
45S
180
90W
0
90E
180
5
10
20
30
40

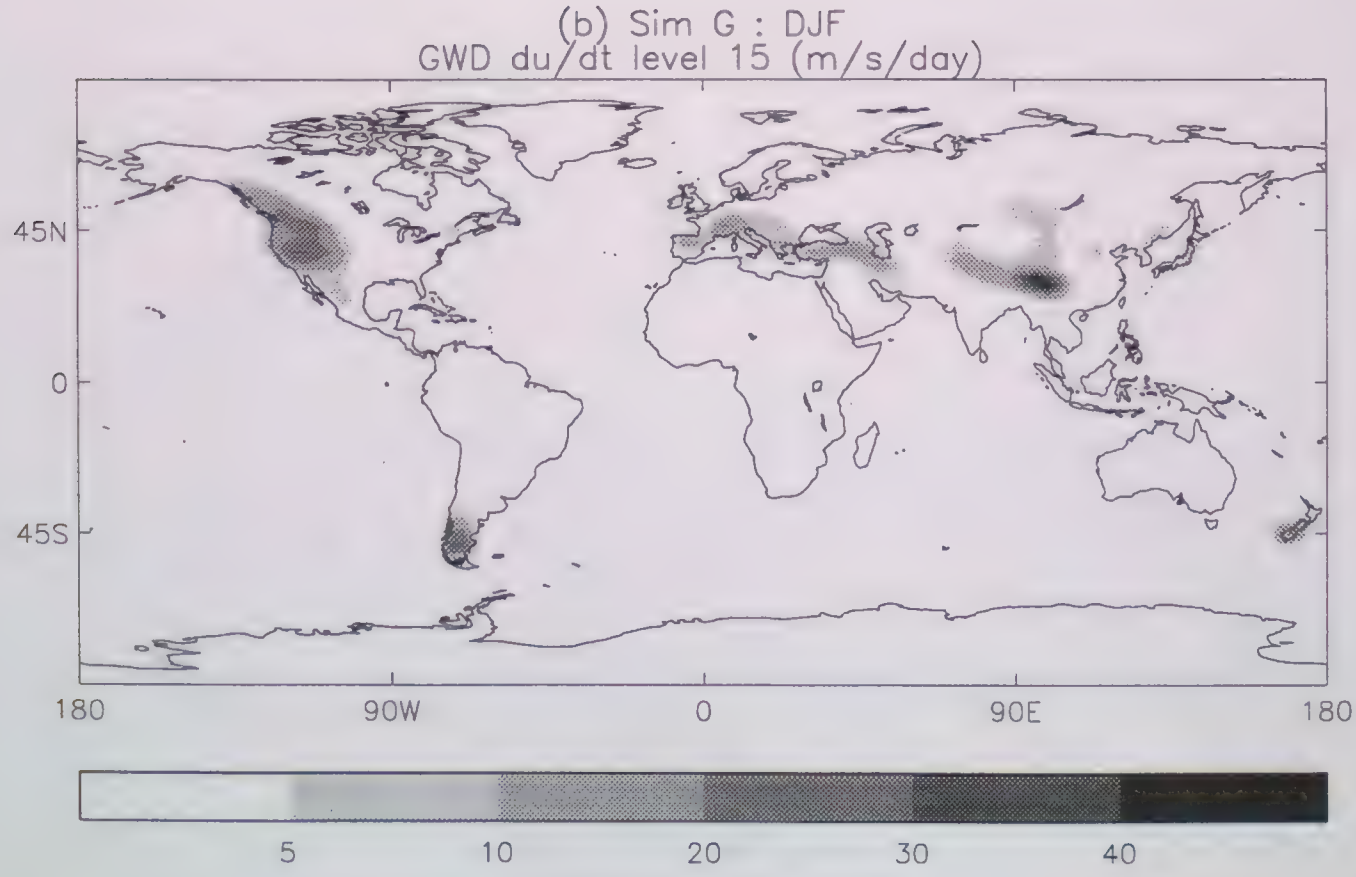
(b) Sim G : DJF
GWD du/dt level 15 (m/s/day)
45N
0
45S
180
90W
0
90E
180
5
10
20
30
40

Figure 6

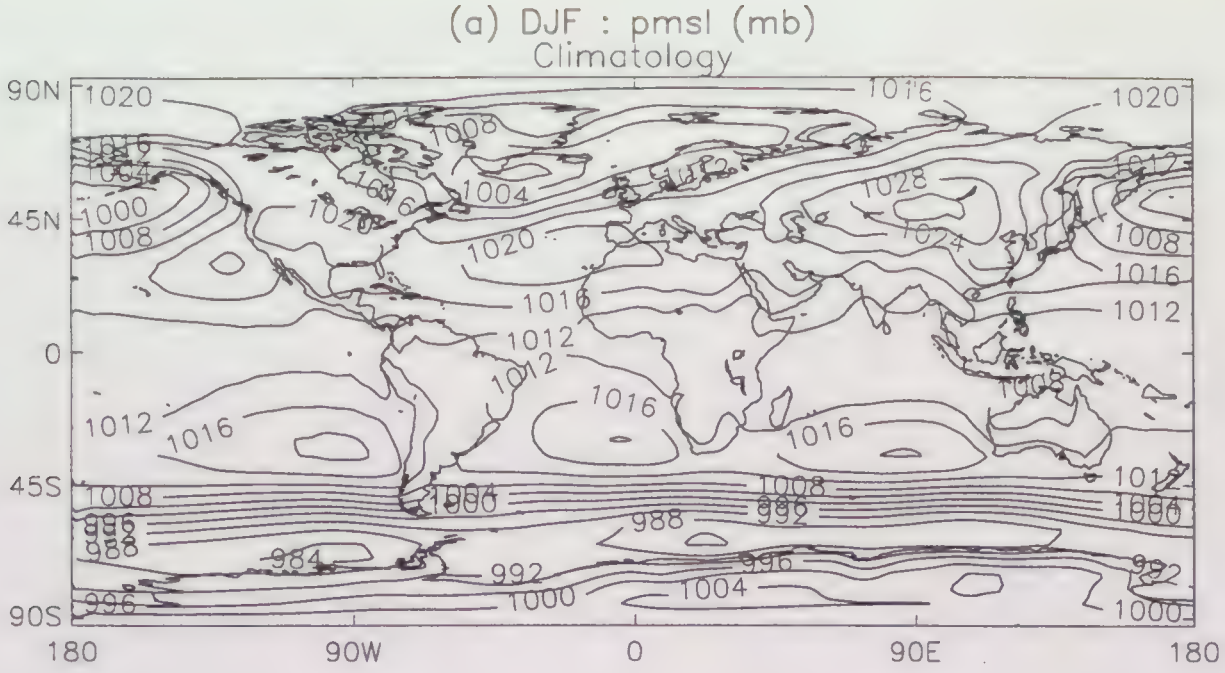
(a) DJF : pmsl (mb)
Climatology
90N
45N
0
45S
90S
180
90W
0
90E
180

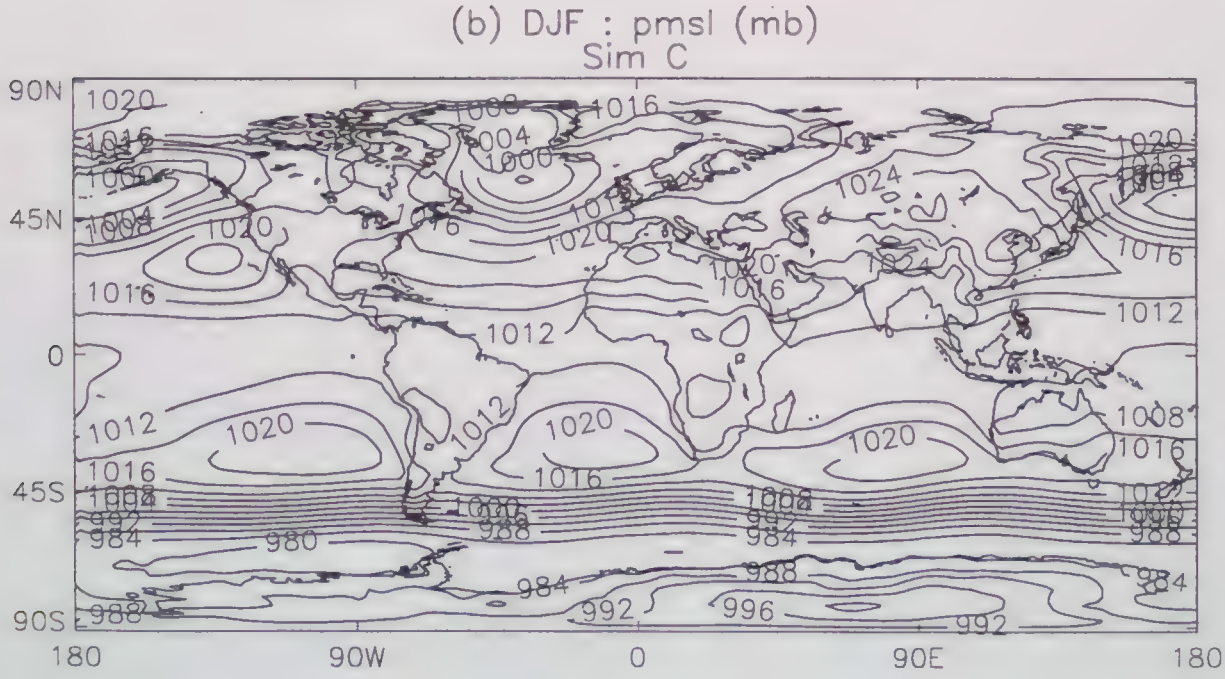
(b) DJF : pmsl (mb)
Sim C
90N
45N
0
45S
90S
180
90W
0
90E
180

Figure 7

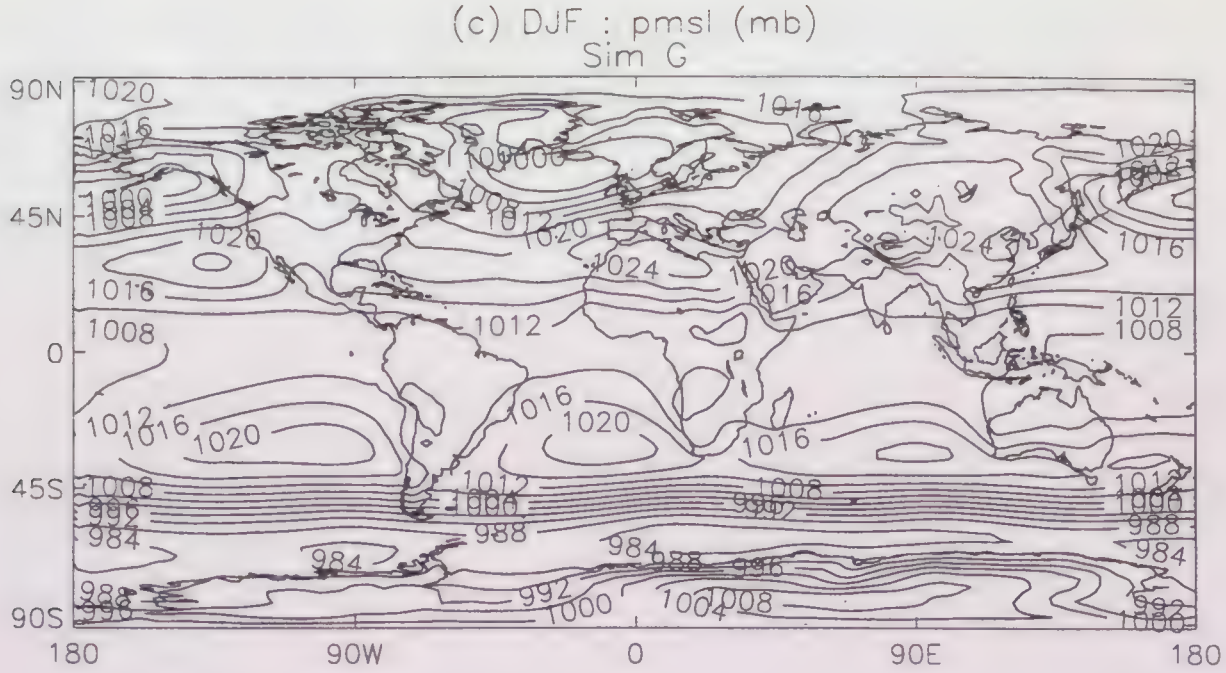

Figure 7 contd

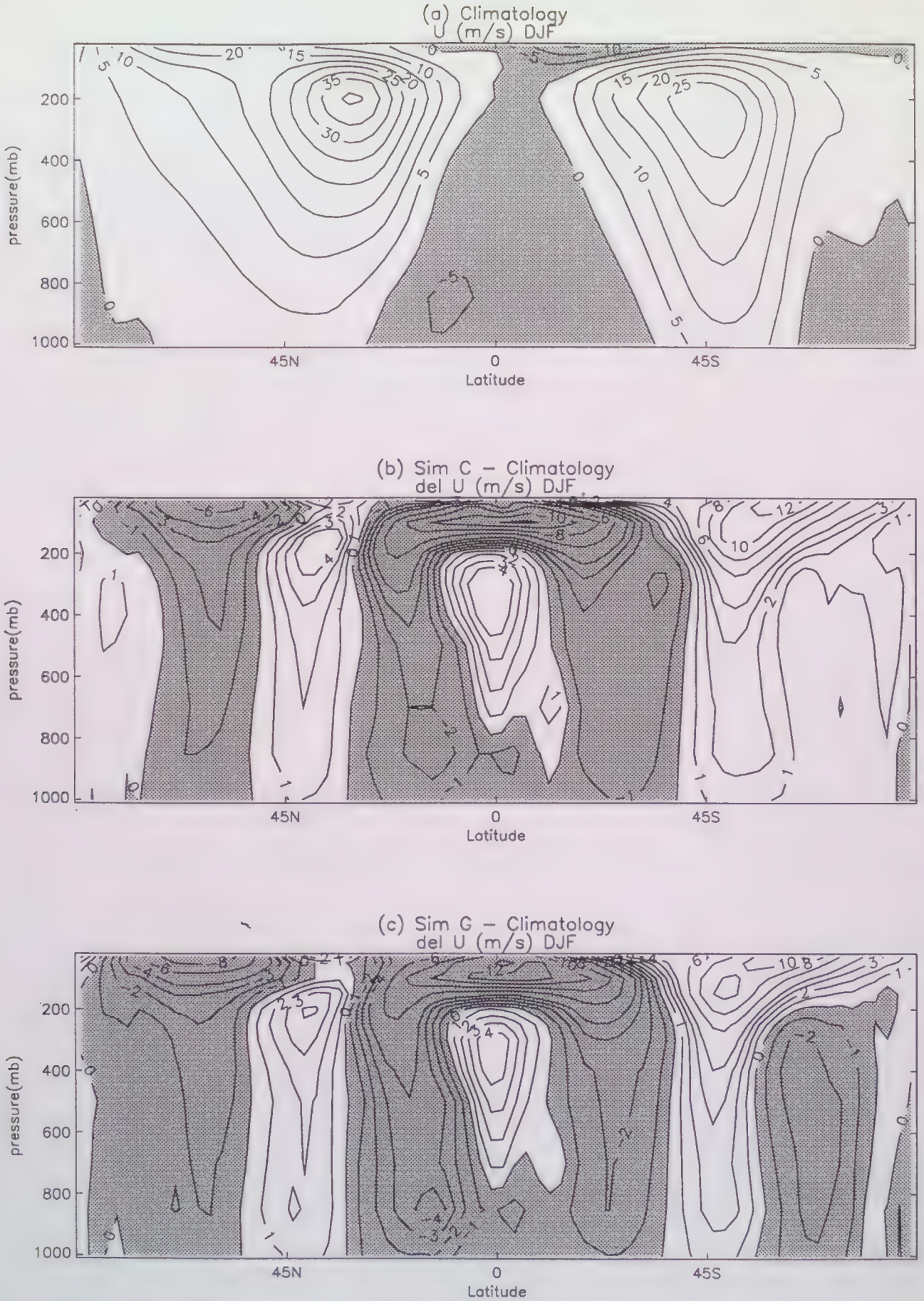
(a) Climatology
U (m/s) DJF
pressure(mb)
200
400
600
800
1000
45N
0
45S
Latitude
(b) Sim C – Climatology
del U (m/s) DJF
pressure(mb)
200
400
600
800
1000
45N
0
45S
Latitude
(c) Sim G – Climatology
del U (m/s) DJF
pressure(mb)
200
400
600
800
1000
45N
0
45S
Latitude

Figure 8

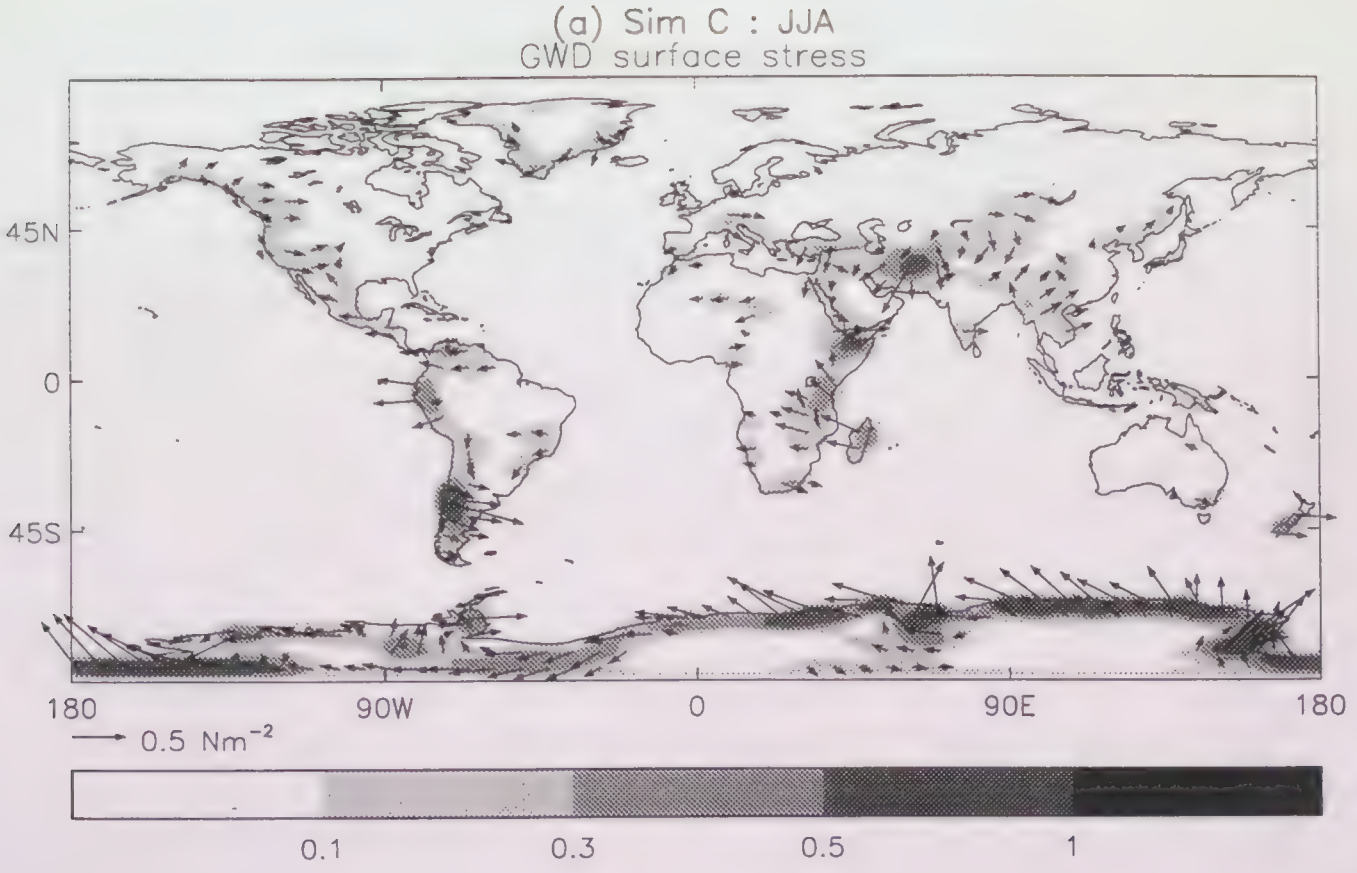
(a) Sim C : JJA
GWD surface stress
45N
0
45S
180
90W
0
90E
180
0.5 Nm⁻²
0.1
0.3
0.5
1

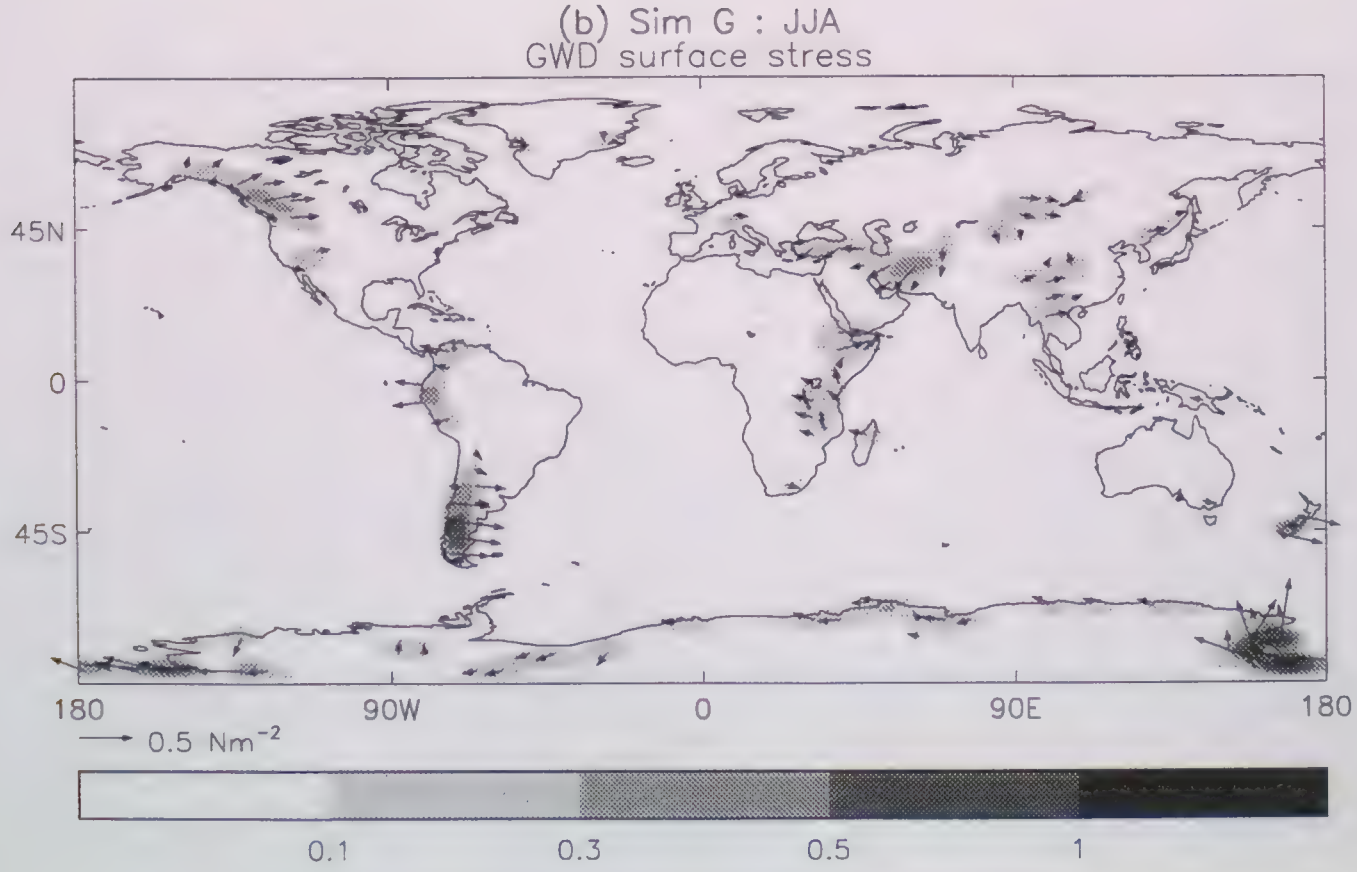
(b) Sim G : JJA
GWD surface stress
45N
0
45S
180
90W
0
90E
180
0.5 Nm⁻²
0.1
0.3
0.5
1

Figure 9

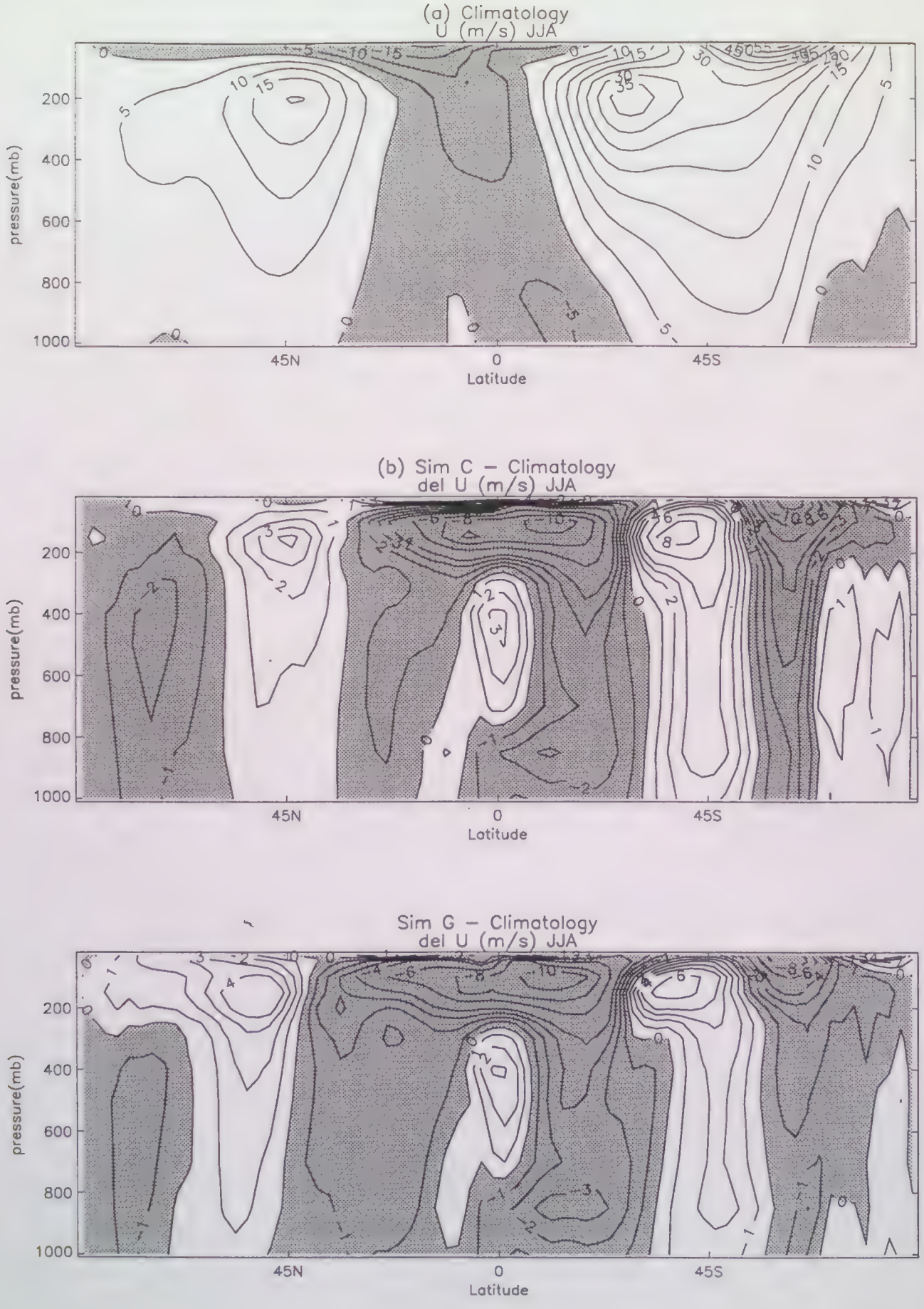
(a) Climatology
U (m/s) JJA
pressure(mb)
200
400
600
800
1000
45N
0
45S
Latitude
(b) Sim C – Climatology
del U (m/s) JJA
pressure(mb)
200
400
600
800
1000
45N
0
45S
Latitude
Sim G – Climatology
del U (m/s) JJA
pressure(mb)
200
400
600
800
1000
45N
0
45S
Latitude

Figure 10

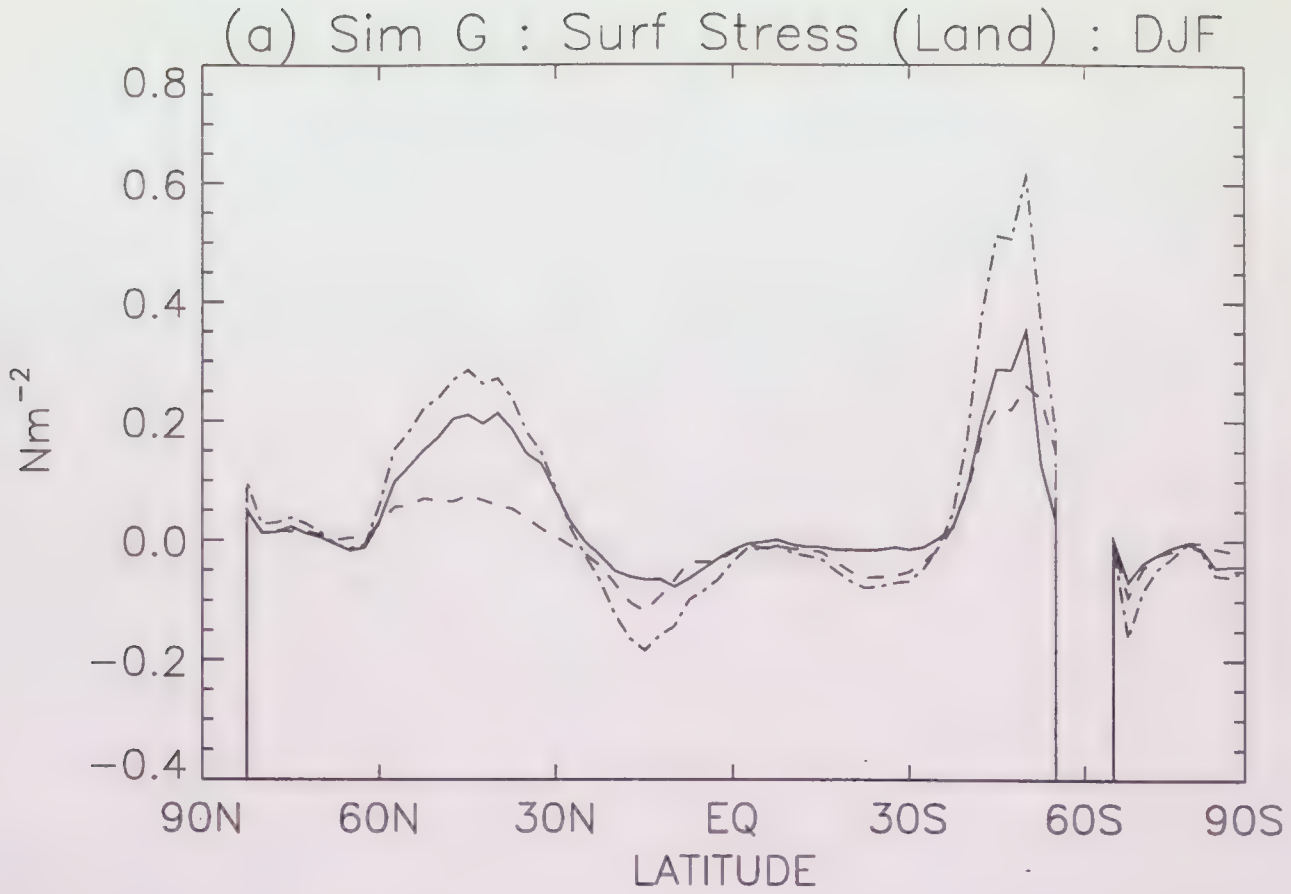
(a) Sim G : Surf Stress (Land) : DJF
0.8
0.6
0.4
0.2
0.0
−0.2
−0.4
Nm⁻²
90N
60N
30N
EQ
30S
60S
90S
LATITUDE

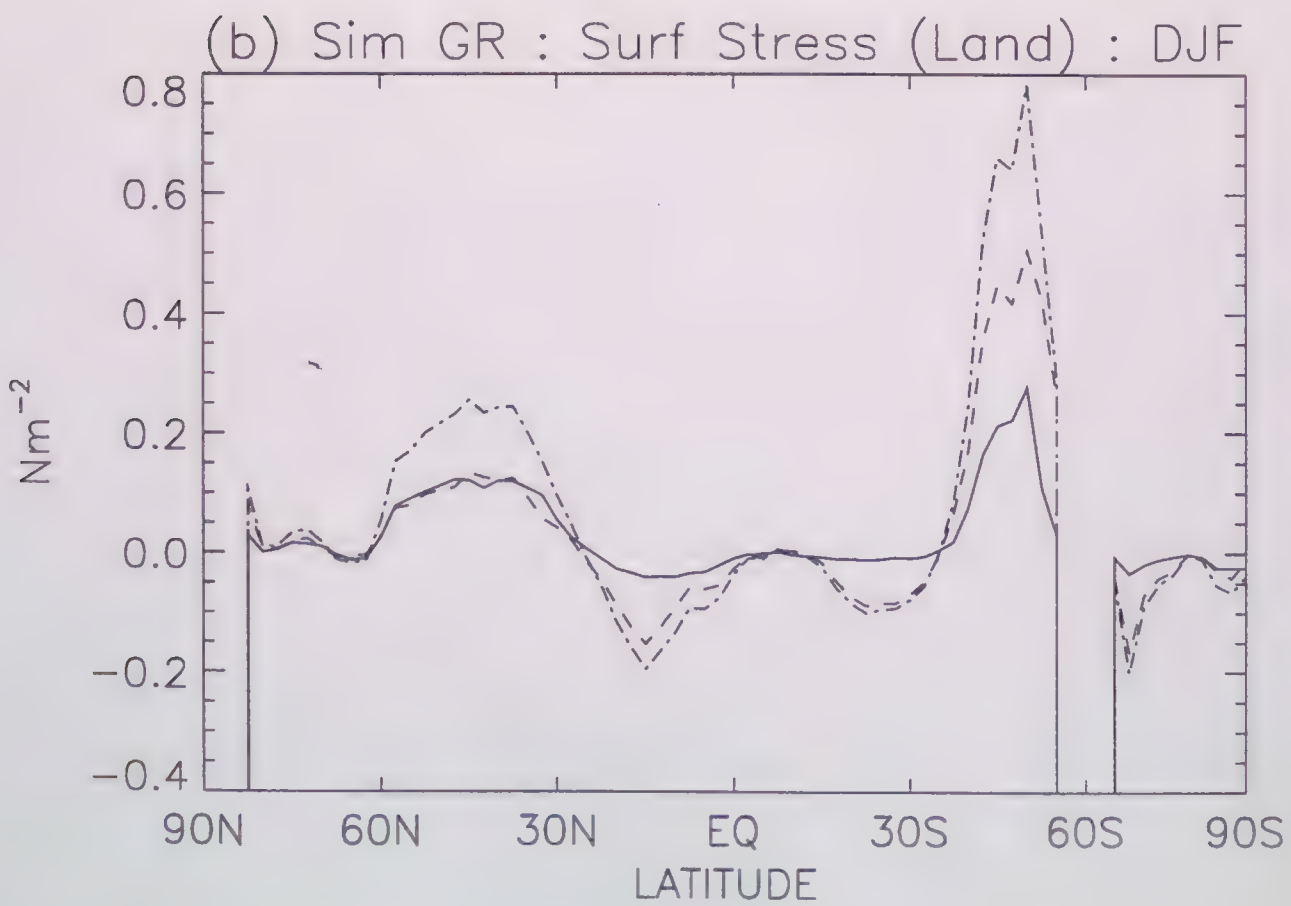
(b) Sim GR : Surf Stress (Land) : DJF
0.8
0.6
0.4
0.2
0.0
−0.2
−0.4
Nm⁻²
90N
60N
30N
EQ
30S
60S
90S
LATITUDE

Figure 11

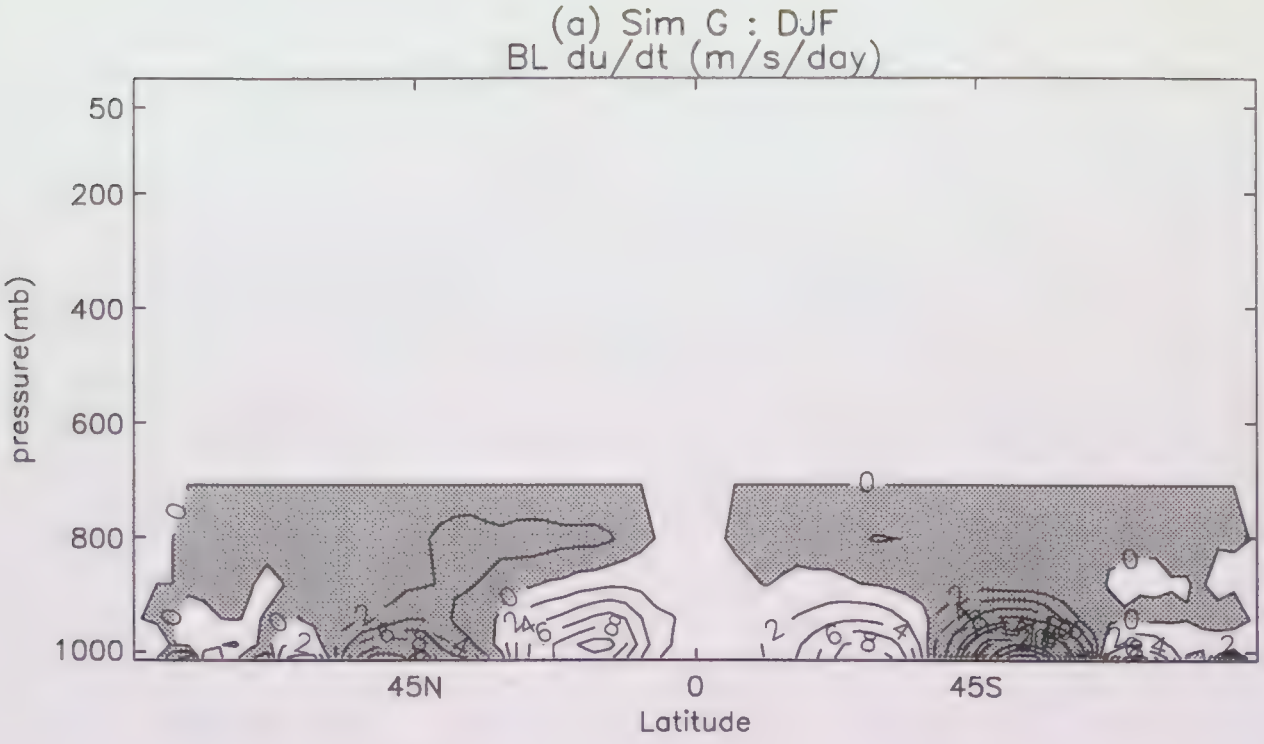
(a) Sim G : DJF
BL du/dt (m/s/day)
50
200
400
600
800
1000
pressure(mb)
45N
0
45S
Latitude

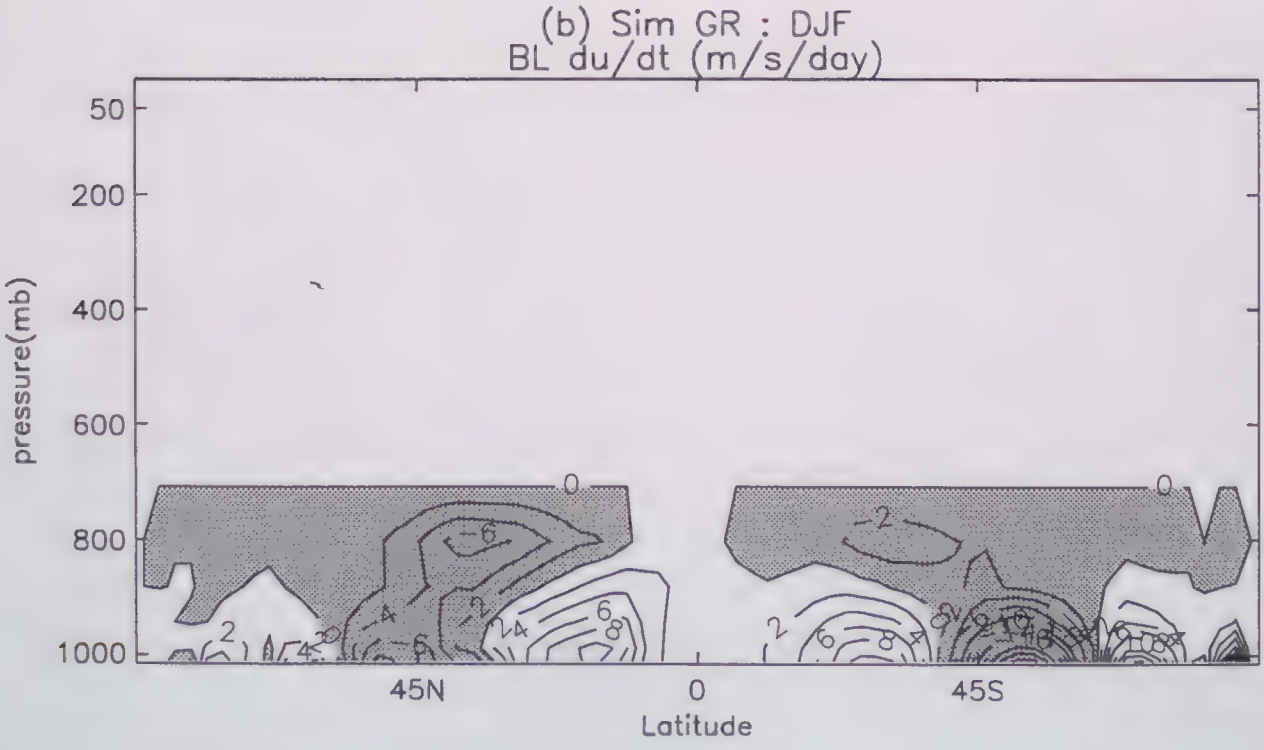
(b) Sim GR : DJF
BL du/dt (m/s/day)
50
200
400
600
800
1000
pressure(mb)
45N
0
45S
Latitude

Figure 12

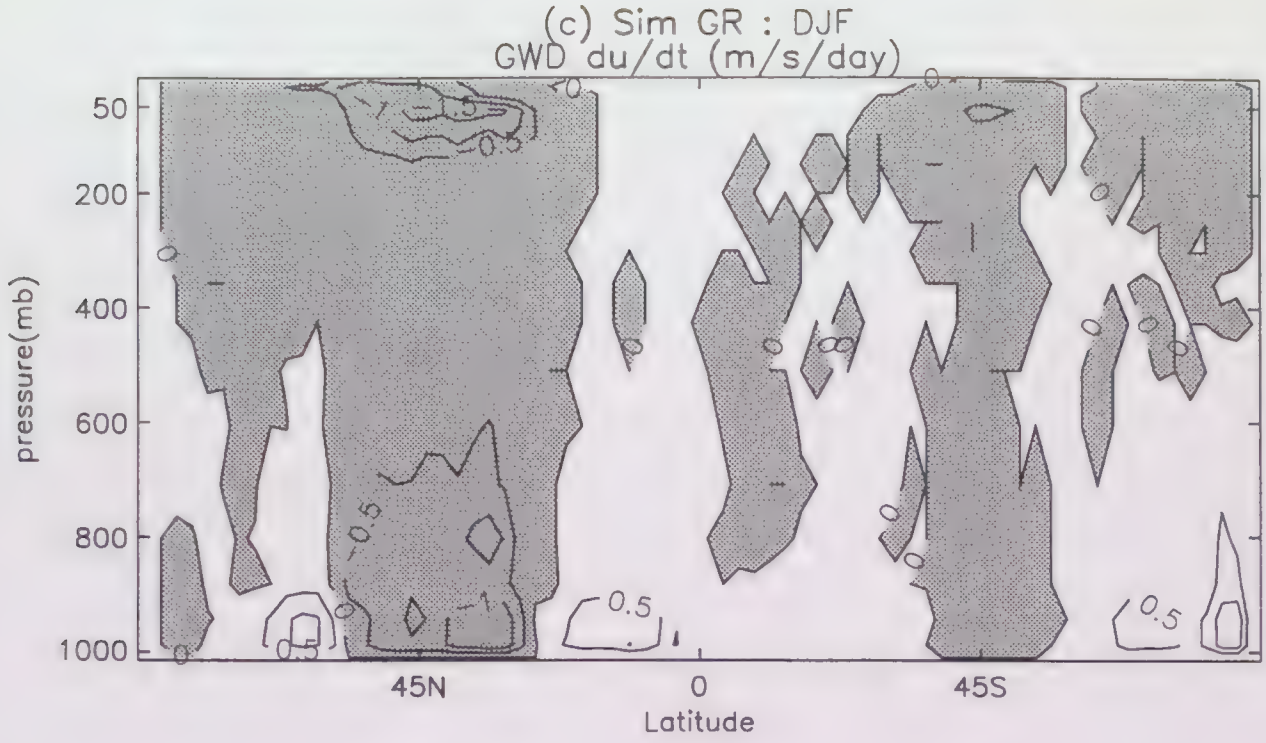

Figure 12 contd

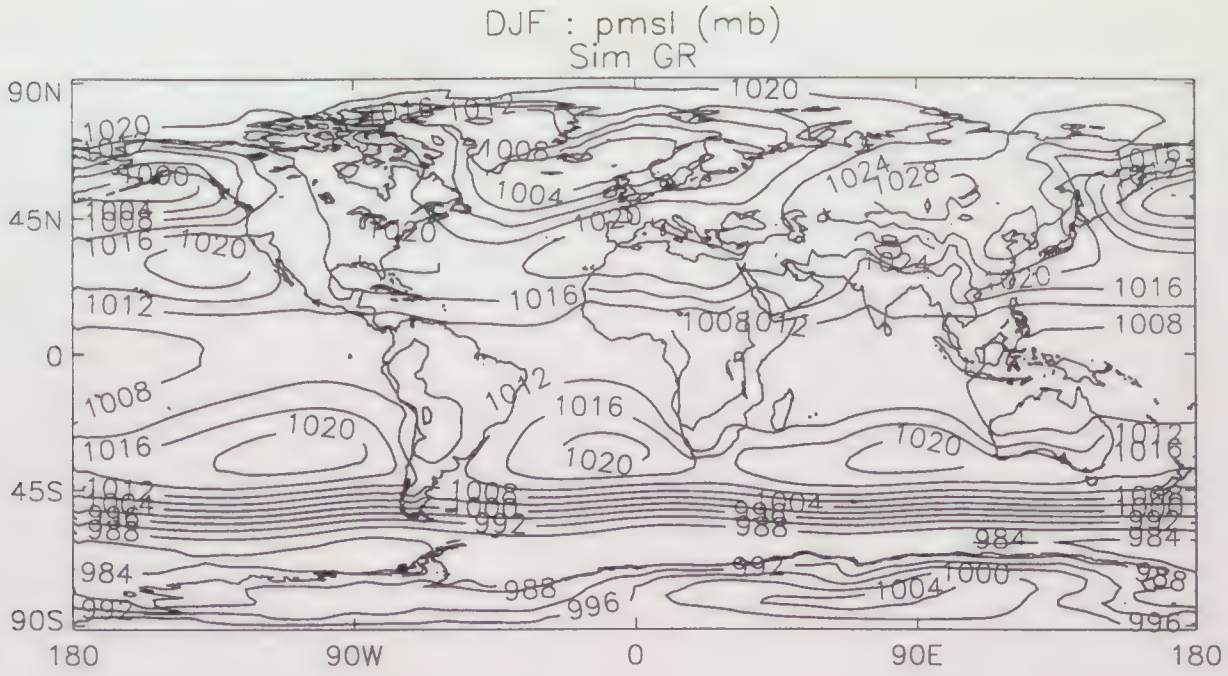
DJF : pmsl (mb)
Sim GR
90N
45N
0
45S
90S
180
90W
0
90E
180
1020
1016
1012
1008
1004
1000
996
992
988
984
1024
1028

Figure 13

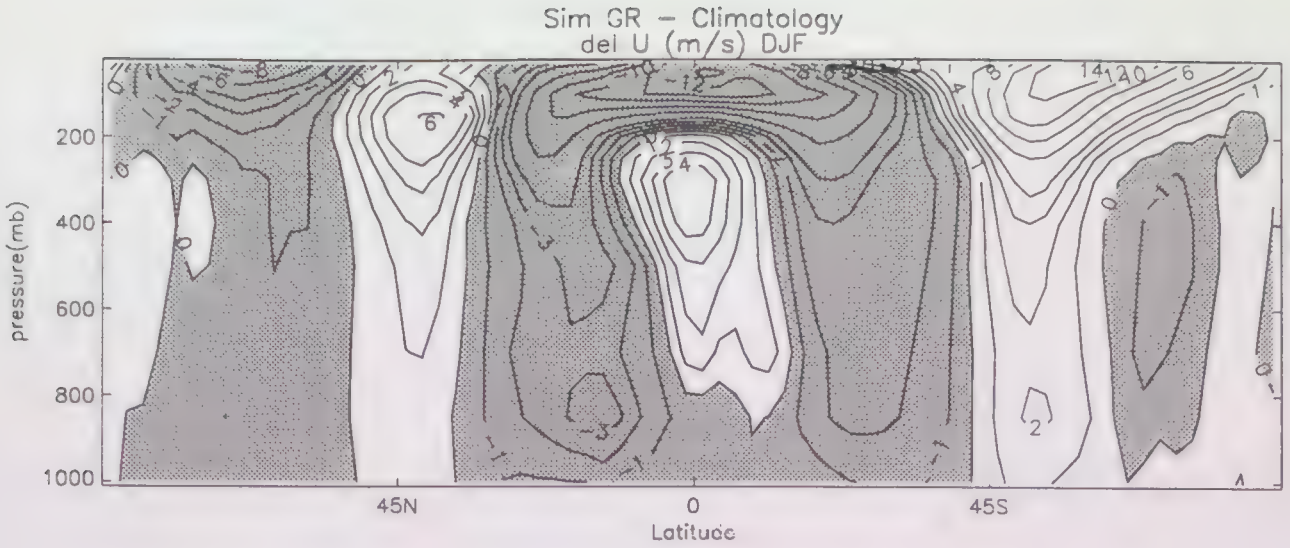
Sim GR – Climatology
del U (m/s) DJF
pressure(mb)
200
400
600
800
1000
45N
0
45S
Latitude

Figure 14

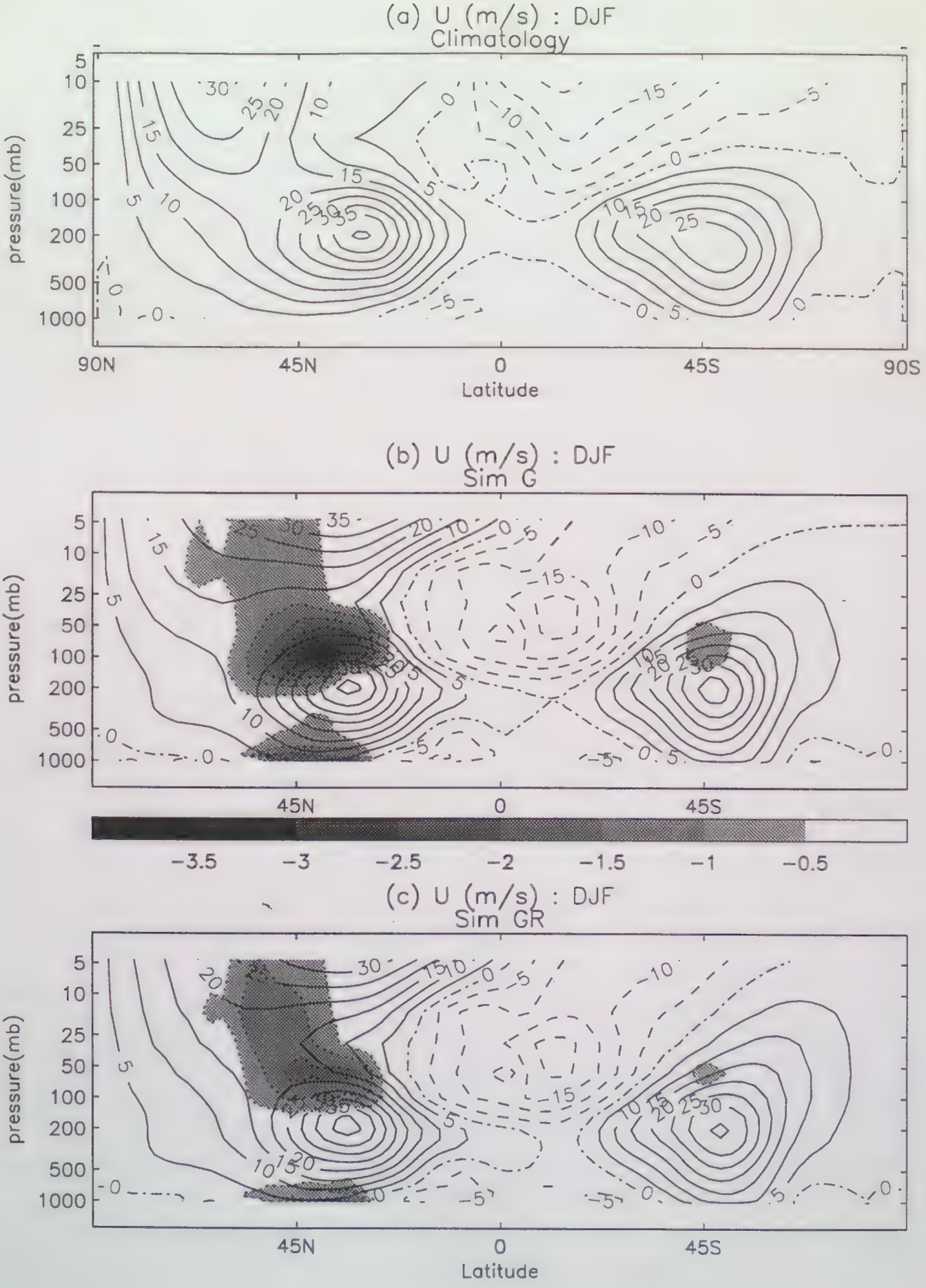
(a) U (m/s) : DJF
Climatology
pressure(mb)
5
10
25
50
100
200
500
1000
90N
45N
0
45S
90S
Latitude
(b) U (m/s) : DJF
Sim G
pressure(mb)
45N
0
45S
−3.5
−3
−2.5
−2
−1.5
−1
−0.5
(c) U (m/s) : DJF
Sim GR
pressure(mb)
45N
0
45S
Latitude

Figure 15

CLIMATE RESEARCH TECHNICAL NOTES

CRTN 1	Oct 1990	Estimates of the sensitivity of climate to vegetation changes using the Penman-Monteith equation. P R Rowntree
CRTN 2	Oct 1990	An ocean general circulation model of the Indian Ocean for hindcasting studies. D J Carrington
CRTN 3	Oct 1990	Simulation of the tropical diurnal cycle in a climate model. D P Rowell
CRTN 4	Oct 1990	Low frequency variability of the oceans. C K Folland, A Colman, D E Parker and A Bevan
CRTN 5	Dec 1990	A comparison of 11-level General Circulation Model Simulations with observations in the East Sahel. K Maskell
CRTN 6	Dec 1990	Climate Change Prediction. J F B Mitchell and Qing-cun Zeng
CRTN 7	Jan 1991	Deforestation of Amazonia - modelling the effects of albedo change. M F Mylne and P R Rowntree
CRTN 8	Jan 1991	The role of observations in climate prediction and research. D J Carson
CRTN 9	Mar 1991	The greenhouse effect and its likely consequences for climate change. D J Carson
CRTN 10	Apr 1991	Use of wind stresses from operational N.W.P. models to force an O.G.C.M. of the Indian Ocean. D J Carrington
CRTN 11	Jun 1991	A new daily Central England Temperature series, 1772-1991. D E Parker, T P Legg and C K Folland
CRTN 12	Jul 1991	Causes and predictability of Sahel rainfall variability. D P Rowell, C K Folland, K Maskell, J A Owen, M N Ward

CLIMATE RESEARCH TECHNICAL NOTES

CRTN 13	Jul 1991	Modelling changes in climate due to enhanced CO2, the role of atmospheric dynamics, cloud and moisture. C A Senior, J F B Mitchell, H Le Treut and Z-X Li
CRTN 14	Sep 1991	Sea temperature bucket models used to correct historical SST data in the Meteorological Office. C K Folland
CRTN 15	Aug 1991	Modelling climate change, and some potential effects on agriculture in the U.K. P R Rowntree, B A Callander and J Cochrane
CRTN 16	Aug 1991	The Boreal Forests and Climate G Thomas and P R Rowntree
CRTN 17	Aug 1991	Development of a Stratosphere-Troposphere Data Assimilation System. R Swinbank.
CRTN 18	Sep 1991	A study of asynchronous coupling using a simple climate model. M K Davey.
CRTN 19	Sep 1991	The Oceanic Carbon Cycle. N K Taylor
CRTN 20	Nov 1991	Worldwide ocean-atmosphere surface fields in Sahel wet and dry years using provisionally corrected surface wind data. M N Ward
CRTN 21	Dec 1991	Coupled tropical ocean global atmosphere models at the UKMO. M K Davey, C Gordon, S Ineson and S Lawrence
CRTN 22	Dec 1991	Empirical parameterisation of tropical ocean-atmosphere coupling. M Allen, M K Davey, D L T Anderson and P D Killworth
CRTN 23	Feb 1992	The temporal evolution of Equatorial Currents in the Indian Ocean D L T Anderson, D J Carrington, R A Corry and C Gordon
CRTN 24	Feb 1992	Stratospheric analyses provided by the U.K. Meteorological Office M J Bailey, A O'Neill and V D Pope

CLIMATE RESEARCH TECHNICAL NOTES

CRTN 25	Feb 1992	Modelling interannual variability in the Indian Ocean using momentum fluxes from the UKMO and ECMWF operational weather analyses. D L T Anderson and D J Carrington
CRTN 26	Mar 1992	A GCM simulation of the impact of Amazonian deforestation on climate using an improved canopy representation J Lean and P R Rowntree
CRTN 27	Mar 1992	The parameterization of rainfall interception in GCMs A J Dolman and D Gregory
CRTN 28	Jun 1992	Development of worldwide marine data eigenvectors since 1985 A W Colman
CRTN 29	Jun 1992	A tropical ocean model with reduced physics M K Davey
CRTN 30	Jun 1992	International Temperature Workshop, Boulder, Colorado, USA, 16 January 1992 Edited by D E Parker
CRTN 31	Jul 1992	Simulation of clear-sky outgoing longwave radiation over the oceans using operational analyses A Slingo and M J Webb
CRTN 32	Sep 1992	A prediction of the transient response of climate J M Murphy
CRTN 33	Nov 1992	LEPS scores for assessing climate model simulations and long-range forecasts. C K Folland
CRTN 34	Jan 1993	Stratospheric Data Assimilation System Guide Editer: R Swinbank
CRTN 35	Mar 1993	A Stratosphere-Troposphere Data Assimilation System R Swinbank and A O'Neill
CRTN 36	Mar 1993	Validation of hydrological schemes for climate models against catchment data. P R Rowntree and J Lean

CLIMATE RESEARCH TECHNICAL NOTES

CRTN 37	Apr 1993	Modelling of palaeoclimates: Examples from the recent past J F B Mitchell
CRTN 38	May 1993	A simulation of seasonality in ENSO forecast skill M K Davey, D L T Anderson and S Lawrence
CRTN 39	Jul 1993	ENSO Prediction experiments using a simple ocean-atmosphere model D-H Wu, D L T Anderson and M K Davey
CRTN 40	Sep 1993	Diagnosis of dynamic sea-surface and sea-level changes from the Cox ocean model J M Gregory
CRTN 41	Sep 1993	Seasonal variations of the clear-sky greenhouse effect: the role of changes in atmospheric temperatures and humidities M J Webb, A Slingo and G L Stephens
CRTN 42	Nov 1993	Sea-level changes under increasing atmospheric CO_2 in a transient coupled ocean-atmosphere GCM experiment. J M Gregory
CRTN 43	Dec 1993	Global and regional patterns of climate change: recent predictions for the Arctic P R Rowntree
CRTN 44	Feb 1994	The effect of changing horizontal diffusion in the atmospheric version of the unified climate model C D Hall and R A Stratton
CRTN 45	Mar 1994	Simulation of El-Niño/Southern Oscillation like variability in a global AOGCM and its response to CO_2 increase. S F B Tett
CRTN 46	Apr 1994	Global data required for monitoring climate change. D E Parker and C K Folland
CRTN 47	May 1994	Seasonal uptake of anthropogenic CO_2 in an ocean general circulation model. N K Taylor

CLIMATE RESEARCH TECHNICAL NOTES

CRTN 48	Jun 1994	A tropic-wide oscillation of boreal summer rainfall and patterns of sea-surface temperature. M N Ward, K Maskell, C K Folland, D P Rowell and R Washington
CRTN 49	Jun 1994	Simulation of the tropical Pacific using a simplified ocean model M A Balmaseda, D L T Anderson and M K Davey
CRTN 50	Sep 1994	Simulation of global mean temperature using a box-diffusion climate model P R Rowntree
CRTN 51	Sep 1994	Seasonal dependence of ENSO prediction skill M A Balmaseda, M K Davey and D L T Anderson
CRTN 52	Nov 1994	Simulation of the Indian Monsoon and Tropical Intraseasonal Variability by a General Circulation Model P M Inness and D Gregory
CRTN 53	Mar 1995	A comparison of modelled surface fluxes with climatological estimates. C Gordon and D K Wright
CRTN 54	Mar 1995	The representation of moist convection in atmospheric models. D Gregory
CRTN 55	Mar 1995	A consistent treatment of the evaporation of rain and snow for use in large-scale models D Gregory
CRTN 56	Apr 1995	Workshop on simulations of the Climate of the Twentieth Century using GISST, 28-30 November 1994, Hadley Centre, Bracknell, UK Edited by C K Folland and D P Rowell
CRTN 57	May 1995	Enhanced shortwave cloud radiative forcing due to anthropogenic aerosols. S E Swartz and A Slingo
CRTN 58	May 1995	The simulation of the tropical oceans in models of different horizontal resolution. C Gordon, D K Wright and C M Roberts
CRTN 59	Sep 1995	The water budget of middle latitude continental regions - a modelling and observational study P R Rowntree
CRTN 60	Sep 1995	Intraseasonal variability of the Indian summer monsoon simulated by the Hadley Centre climate model K Ashok, D Gregory and P M Inness

CLIMATE RESEARCH TECHNICAL NOTES

CRTN 61	Sep 1995	Climate simulations with the Unified Model: AMIP runs C D Hall, R A Stratton and M L Gallani
CRTN 62	Nov 1995	Validation of surface parameters over the oceans in climate simulations with the unified model. C D Hall
CRTN 63	Dec 1995	The GISST2.2 sea surface temperature and sea-ice climatology D E Parker, M Jackson and E B Horton
CRTN 64	Dec 1995	Parametrization of momentum transport by convection. II: Tests in single column and general circulation models. D Gregory, R Kershaw and P M Inness
CRTN 65	Jan 1996	Understanding the sensitivity of a GCM simulation of Amazonian deforestation to the specification of vegetation and soil characteristics. J Lean and P R Rowntree
CRTN 66	Jan 1996	On the efficient calculation of infra-red fluxes and cooling rates using the two-stream equations. J M Edwards
CRTN 67	Jan 1996	The second Hadley Centre coupled ocean-atmosphere GCM: Model description, spinup and validation. TC Johns,RE Carnell,JF Crossley,JM Gregory, JFB Mitchell,CA Senior,SFB Tett and RA Wood
CRTN 68	Feb 1996	The sensitivity of climate simulations to the specification of mixed phase clouds D Gregory and D Morris
CRTN 69	Apr 1996	Using an ensemble of Multi-Decadal GCM simulations ro assess potential seasonal predictability D P Rowell
CRTN 70	May 1996	North Atlantic and European Seasonal Predictability using an Ensemble of Multi-Decadal AGCM Simulations J R Davies, D P Rowell and C K Folland
CRTN 71	Jun 1996	A description of the Second Hadley Centre Coupled Model (HADCM2) T C Johns
CRTN 72	Jul 1996	Palaeoclimate Modelling Intercomparison: UKMO GCM simulations for 6kBP and 21kBP C D Hewitt and J F B Mitchell

CLIMATE RESEARCH TECHNICAL NOTES

CRTN 73	Aug 1996	ENSO responses and low frequency weather variability in the North Pacific/American sector 1949-93 A C Renshaw, D P Rowell and C K Folland
CRTN 74	Sep 1996	Version 2.2 of the Global sea-Ice and Sea Surface Temperature data set, 1903-1994 N A Rayner, E B Horton, D E Parker, C K Folland and R B Hackett
CRTN 75	Sep 1996	A new gravity wave drag scheme incorporating anisotropic orography and low level wave breaking : Impact upon the climate of the UK Met Office Unified Model D Gregory, G J Shutts and J R Mitchell